Drops, jets and high-resolution 3D printing: Fundamentals and applications

Richard Caulfield[1*], Feihuang Fang[1*] and Manish K. Tiwari[1,2†]

[1]Nanoengineered Systems Laboratory, UCL Mechanical Engineering, University College London, Torrington Place, London WC1E 7JE, United Kingdom

[2]Wellcome EPSRC Centre for Interventional and Surgical Sciences (WEISS), University College London, London, United Kingdom

Abstract: The ability to print high-resolution (< 10 μm) three-dimensional (3D) features is important in numerous existing and emerging applications such as tissue engineering, nanoelectronics, photovoltaics, optics, biomedical devices etc. The current chapter is focused on a sub-set of high-resolution printing techniques that exploit micro and nanofluidics features to attain high resolution. Here these approaches are referred as fluidics assisted high-resolution 3D printing. Salient examples of such techniques are electrohydrodynamic printing, direct-write assembly, aerosol jet printing, etc. The chapter starts with a brief introduction and discussion on the challenges of high-resolution printing. This is followed by a section on fundamental mechanisms of droplet, jet and filament formations, and their role in deciding the print resolution. Commonalities between different printing techniques (e.g. the physics of jet breakup and role of capillary stresses) are highlighted in order to provide a systematic understanding and context. Next the fluid mechanics features determining the print resolution and quality are discussed in detail. This includes sections on the role of ink rheology, evaporation rate, nozzle size, substrate and nozzle wetting properties (i.e. surface energy) and dynamic effects such as drop impact and spreading, stability of printed liquid lines and liquid filaments etc. Wherever relevant, literature on much more established inkjet printing techniques is also exploited to provide a context for the high-resolution printing and clarify the distinct benefits and challenges that emerge at progressively higher resolutions. In the wetting and surface energy section, features of dip-pen lithography and transfer printing, two popular techniques for two-dimensional high-resolution printing, are also briefly introduced for completeness. Lastly, the chapter ends with a summary and brief perspective on future research trends in this area.

* These authors contributed equally to this work.

† Corresponding Author. Phone: +44 (0)20 3108 1056. Email: m.tiwari@ucl.ac.uk

Chapter outline

1. **Introduction**
   1.1. Challenges of high-resolution printing
2. **Fundamentals: droplets, jets and filaments in printing**
   2.1. Droplets and jets: electrohydrodynamic printing
      2.1.1. Nano-dripping
      2.1.2. E-jetting
   2.2. Meniscus transport: Dip-pen nanolithography
   2.3. Filaments: direct-write (DW) printing
   2.4. Nozzle-less printing
      2.4.1. Pyroelectrohydrodynamic printing
      2.4.2. Laser-induced forward transfer (LIFT) printing
   2.5. Transfer printing
3. **Fluid mechanics features**
   3.1. Ink rheology and pressure drop
   3.2. Substrate wetting
   3.3. Nozzle properties
      3.3.1. Nozzle size
      3.3.2. Nozzle wetting
   3.4. Dynamic effects
4. **Exemplar demonstrations of high-resolution printing**
   4.1. Direct-write printing
   4.2. EHD printing
   4.3. Hybrid techniques
   4.4. Nozzle-less printing
   4.5. Transfer printing
   4.6. Dip-pen nanolithography
5. **Summary and perspective**
6. **Bibliography**

1. Introduction

Rapid prototyping and simplifying manufacturing processes and supply chains are some of the key features that have elicited exceptional interest in 3D printing technologies. In recent time, considerable progress has been made to extend these approaches to print at high-resolution (<10 μm) with progressively increasing diversity of materials being printed for a wide variety of applications ranging from flexible and wearable electronics to a new generation of photonics and implantable devices [1-3]. In this chapter, we will focus on a sub-set of these techniques that exploit micro and nanoscale fluidics and discuss the features that are used to enable high-resolution 3D printing. We will begin with a summary of the challenges of such fluidics assisted high-resolution 3D printing and the progress made towards overcoming them. We will then move on to a discussion on specific features of fluidics assisted printing techniques and the fluidic features that play a role in each. Among the various high-resolution printing techniques exploiting fluidics, electrohydrodynamic (EHD) and direct-write (DW) printing techniques and approaches relying on their hybrid features, are the most well established in terms of high-resolution capability and thus are our primary emphasis. Additionally, we will also briefly cover dip-pen lithography and transfer printing techniques, which share some commonalities in terms of fluidics and wettability features with EHD and DW techniques. Within each technique we will discuss the fluidic features that are exploited and delve into the fundamental mechanisms that underpin them such as droplet formation, jetting and filament formation. Following this, we will look at the fluid mechanical properties that play a key role in deciding the print resolution and quality, e.g. the printing "ink" rheology, evaporation rate, nozzle size, substrate and nozzle wetting properties (surface energy) and dynamic effects (pertaining to liquid-solid interactions which are present in all fluidics assisted printing technologies). We will finish with citing salient applications of the printing techniques introduced and some discussion on future directions in this active research field.

1.1. Challenges of high-resolution 3D printing

There are a number of key challenges that have dogged the development of high-resolution printing. Firstly, such printing often requires flow through small capillaries and channels, where the pressure drop scales with $\sim D^4$ (Poiseuille relationship, c.f. Equation 3.3 below)[4], with D being the relevant length scale, e.g. the diameter of the printing nozzles. This implies a 16-fold increase in pressure drop when halving the nozzle diameter. Thus, for same flow rate, going down from ~10 μm to ~1 μm will entail a four orders of magnitude increase in the pressure drop.
Secondly, at small scales the capillary (interfacial) and wettability effects are highly dominant and must be carefully controlled[5]. This implies a control of wettability (often at microscale) of both the dispenser (e.g. nozzles, tips, or printing stamps) and the substrate, which is non-trivial.

Thirdly, evaporation of a liquid scales with surface area; for example, for a sessile droplet this will imply ~d_c^2 scaling, where d_c is the contact diameter (see section 3.4)[6]. This implies that inks formulated for standard inkjet printing (with minimal nozzle diameters of ~ 10 μm), run into serious clogging issues when used in high-resolution printing. Often, for stability of the printed structures, a higher-evaporation rate is required post processing. This increases the solid content of the printed features, raising their local elastic moduli and stability[7, 8]. However, this requirement is at odds with the evaporation-led nozzle clogging. In fact, for some techniques, such as direct-write printing, thick inks with a shear thinning property are desirable. This naturally, requires a careful formulation of the ink, which is non-trivial.

Last but not least, often exploitation of high-resolution printed structures relies on their integration on existing devices and application-specific substrates. This poses a materials challenge and packaging issues, which are not unlike what the microelectronic industry has faced for a long time. Whereas this has not stopped major early inroads to demonstrate the exciting potential of high-resolution 3D printing, on-demand and site-specific deposition of material on 3D substrates encountered, for example, in healthcare engineering applications, continues to remain an important challenge to overcome.

2. Fundamentals: droplets, jets and filaments in printing

In this section, we will discuss the mechanisms of droplet, jet and filament formation which underpin the fluidics assisted high-resolution 3D printing. The benefits of each of the mechanisms are also discussed along with how each one is used in high-resolution 3D printing techniques. A brief introduction to each of the printing techniques mentioned is also given for fullness.

2.1. Droplets and jets: electrohydrodynamic printing

Electrohydrodynamic (EHD) printing uses electric fields to eject ink through printing nozzles and achieve high-resolution 3D printing [9]. The nozzles used typically have inner diameters in the range of 100 nm to several μm. As required, pneumatic backpressure can be employed to help force the ink to the nozzle tip, where a meniscus forms. The surface tension of the ink allows the meniscus to hold its shape at the tip of the nozzle. An electric field is then applied between the nozzle and the substrate to be printed on (see Fig. 2.1A). The electric field is applied by inserting a metallic wire into the nozzle capillary or by coating the nozzles with a thin layer of metal (usually gold) [9]. The electric field causes movement of the ions in the ink and results in a build-up of mobile ions on the surface of the meniscus [10]. This accumulation of ions in the meniscus leads to an increase in concentration of Maxwell stress in this area. As the electric field increases, so too does the Maxwell stress. The Maxwell stress acts against the surface tension (capillary) stress and causes a deformation of the meniscus into a pointed shape. At a threshold value, the Maxwell and the capillary stresses will be balanced (there is also a small, negligible contribution from gravity)

$$F_{Maxwell} - F_{surface\ tension} + F_{gravity} = 0 \tag{2.1}$$

Above this threshold value the Maxwell stress overcomes the capillary stress of the inks and material begins to be ejected and deposited on the substrate underneath [11].

The detailed physics of ink ejection from the nozzle and drop formation is complex and still under investigation. In fact, as will be discussed later in this section, depending on the field strength and the ink properties, a number of different liquid ejection modes are observed (see Fig. 2.1B) [12-14]. Fortunately, a good understanding of the ink ejection physics can be gained by analysing various time scales involved in EHD printing, such as the droplet formation time, the time of liquid supply to the droplet and the charge relaxation time.

Clearly, to achieve the minimal amount of ink ejection (a single droplet) the characteristic time of liquid supply (τ_q) must be greater than the characteristic time of droplet formation (τ_d) [15]. Put simply, the droplet must have enough time to form before more material flows to the ejection point, i.e.,

$$\tau_q > \tau_d \tag{2.2}$$

In the limit that Equation 2.2 is valid, the time between droplet ejections can be calculated by dividing the droplet volume by the volumetric flow rate (Q) through the nozzle [15], which is controlled by the ink feed rate to the nozzle, as

$$\tau_q = \frac{\pi d^3}{6Q} \tag{2.3}$$

where d is the droplet diameter. Note that by replacing the drop diameter with nozzle diameter in Equation 2.3 we can obtain the time scale for liquid supply to maintain the meniscus forming at the nozzle tip, τ_Q.

The characteristic time of droplet formation can be determined by balancing the surface tension force with the viscous forces. A liquid element will tend to deform to minimise surface area – by forming a droplet – due to surface tension; viscous forces will resist the liquid deformation. The resulting time scale for drop formation can be expressed as [15]

$$\tau_d = \frac{\mu d}{\gamma} \tag{2.4}$$

where μ is the dynamic viscosity of the fluid, d is the droplet diameter and γ is the fluid surface tension.

Therefore, from Equation 2.2, for droplet formation we have

$$Q < \frac{\pi d^2 \gamma}{6\mu} \tag{2.5}$$

Equation 2.5, clearly provides an upper limit on the volume flow rate in case dropwise printing is desired. If on the other hand, $\tau_d > \tau_q$ the liquid ejection rate is too quick to form a droplet and thus ejection should occur in a continuous jetting mode [15].

In EHD printing the liquid ejection is controlled by the ink feed rate, the strength of the applied field and the ink properties. The imposed electric field introduces charges (ions) in the ink. The motion of the charges across the ink meniscus is controlled by the ink conductivity and dielectric strength. It is convenient to think of the movement of charges in a dielectric liquid medium (ink) in terms of their relaxation time (τ_ε), which is defined as the time it takes for ions to move across the dielectric to reach the surface [15]. This charge relaxation time can be expressed as

$$\tau_\varepsilon = \frac{\varepsilon}{\sigma} \tag{2.6}$$

where ε is the electrical permittivity of the ink and σ its electrical conductivity.

Low charge relaxation time relative to the time for liquid supply (τ_q) can facilitate charge accumulation at the meniscus surface after voltage application, thereby facilitating a competition between the resulting Maxwell stress and the capillary

stress to facilitate liquid ejection, beyond a critical value of field strength. Under this condition, if a droplet is ejected from the meniscus the Maxwell stress is high enough to sustain the meniscus, thereby facilitating a sustained ejection of liquid from the meniscus. If on the other hand, the charge relaxation time is larger than the characteristic time of liquid supply then the instantaneous electrical conduction across the ink is no longer the dominant charge transport method and charge convection takes over. The charges are removed from the surface by liquid convection and the long relaxation time prevents its replenishment via conduction. At this point, charge cannot be brought to the meniscus surface fast enough to maintain the balance of Maxwell stress with the capillary stresses and the meniscus can easily retract after ejection of a drop, which makes the liquid ejection unstable [14, 15]. Liquids with $\tau_\varepsilon < \tau_q$ are referred to as leaky dielectrics.

For leaky dielectrics liquid ejection can be maintained in several different modes [12] depending on the applied electric field strength (see Fig. 2.1B). At low values of field, electric field, liquid ejection occurs through dripping in the form of droplets with size greater than the nozzle size; this is essentially an extension of gravity driven dripping, albeit now assisted by electric field. At higher field, the Maxwell stresses become stronger and the meniscus takes a progressively sharper conical shape with liquid ejection occurring from the cone tip. The ejection at intermediate field strengths (marked by dotted rectangle in Fig. 2.1B) occurs in the form of drops (dripping) or jets with diameter much smaller than the nozzle size (up to an order of magnitude). The dripping mode is referred as micro or nano-dripping (depending on the drop sizes) and the jetting is referred as e-jet. The latter occurs either in the form of a pulsed jet or a steady jet (at stronger field). At even higher field strengths, the jet becomes unstable and uncontrollable, with occurrence of multiple jets being another invariably observed phenomenon. At still higher electric field strengths, complex jetting patterns are observed. At very high electric field strengths atomisation occurs and is the basis of electro-spraying.

The dripping and jetting at 'intermediate' field strengths (dotted rectangle in Fig. 2.1B), however, are controllable and can be used to achieve high-resolution EHD printing. The noteworthy printing regimes are discussed in more detail below.

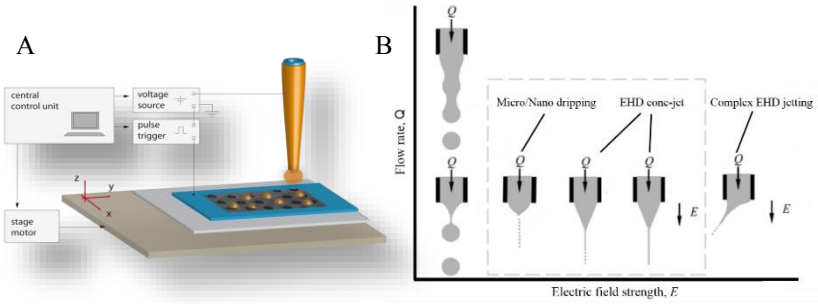

Figure 2.1: (A) Schematic diagram of EHD printing and ink deposition through a customized nozzle under a high-voltage circuit [16], and (B) Formation of electrohydrodynamically induced jets under an applied electric field. Different modes of jetting, depending on the strength of the

electric field and flow rate [9]

2.1.1. Nano-dripping

To form a micro/nano-dripping mode, two conditions have to be met: the characteristic time of supply of liquid to the droplet has to be longer than the characteristic time of drop formation ($\tau_d < \tau_q$) and the relaxation time must be smaller than the time of supply of liquid to meniscus ($\tau_\varepsilon < \tau_Q$). In fact, by appropriately formulating their dilute nanoparticle suspension (ink), Galliker *et al.* [15] were able to achieve stable on-demand dripping from the meniscus at nanoscale (nano-dripping) Fig. 2.1B. To estimate the droplet diameter, d, they evaluated the following balance of surface tension and electric forces numerically [15]

$$\frac{\varepsilon_0}{2}\iint E^2\,(d,V)\cdot da_z = \pi d\gamma \tag{2.7}$$

with E denoting the electric field, V the applied voltage, da_z a differential surface element for the integration over the small hemispherical surface with subscript z denoting the z-direction (from nozzle to substrate), $\boldsymbol{\varepsilon_0}$ and $\boldsymbol{\gamma}$ the permittivity of air and the surface tension, respectively. The integral in the above equation was evaluated by solving for the Maxwell stress tensor in the z-direction followed by integration on the surface of the small pendant droplet. Using 1-μm size nozzles, they were able to achieve sub-100 nm drops.

2.1.2. E-jetting

The second case we will describe is e-jetting, where the ink is ejected in the form of an electric field induced jet. For jetting to occur, the electric field induced Maxwell stress must be much stronger than the capillary stress. This causes the meniscus to become sharply conical, which is known as a Taylor cone. The regime is distinct from the micro/nano-dripping mode, and occurs at higher field strengths. As described above, for jetting, the characteristic time of liquid supply to the droplet (τ_q) must be less than the characteristic time of droplet formation, i.e.,

$$\tau_q < \tau_d \tag{2.8}$$

In fact, as the electric field strength increases beyond micro-nano-dripping, first a stream of ejected material is present. Further inspection reveals that this jet is not a continuous stream and is made up of discrete (larger) droplets released in rapid succession. At this point, a pulsating jet can be created by toggling the electric field on and off, provided that the ink flow and electric field strength are less than that required for a continuous jet (known as the critical or Taylor threshold [9]). At even higher electric field strengths the rate of droplet release increases to give a continuous stream of material jetting from the cone, known as a cone-jet.

For high-resolution printing applications pulsating jets or cone-jets are preferred as they allow a high degree of controllability to deposit material where required. The print resolution achieved using these methods can be as low as ~100 nm [9]. The final print resolution depends on many variables such as the flow rate, the ink properties, the nozzle diameter, the electric field and the distance between the nozzle and the substrate. These aspects will be described later in the chapter.

2.2. Meniscus transport: Dip-pen nanolithography

Using pens to write on paper is one of the earliest methods developed by humankind to create patterns on solid surfaces [17]. There have been many advancements since the days of using quills to write but the basic principles remain the same. The ink is first prepared by mixing solid ink particles with a liquid solvent. The ink is then deposited onto a surface during the writing process. The ink can be transferred from the "pen" either by capillary flow or by applying a back pressure to move it through; regardless of the ink driving mechanism, the ink flow between the pen and the substrate occurs via a liquid bridge (capillary bridge) [18, 19]. After writing, the solvent evaporates out, leaving behind only the solid particles from the ink [17].

Essentially, dip-pen nanolithography uses an atomic force microscope (AFM) tip as the pen to deposit ink directly onto a substrate with nanometre precision. The principle of AFM microscopy differs from optical or electron microscopy as in AFM a sharp tip is moved across the surface to "feel" the bumps and groves [20]. This is referred as the contact mode of AFM imaging. This data can then be analysed to produce visual images similar to those produced in optical or electron microscopy. By using the AFM tip as the pen high-resolution deposition can be achieved.

The dip-pen lithography was pioneered by Mirkin's group [21]. The tip was coated with a molecular ink, similar to how quill pens are coated in ink. When the tip was brought close to the substrate under ambient conditions, water condensed at the AFM tip between the tip and the solid substrate [22], similar to the Kelvin condensation effect in confined geometries with high curvature, thereby forming a liquid bridge between the tip and the substrate. The molecules in the ink then diffuse from the tip down to the substrate where they are deposited in the wake of the tip as it moves along the surface (see Fig. 2.2). By altering variables such as humidity, temperature and tip speed the ink deposition rate and printing resolution can be adjusted to ~10 nm [17].

The molecular diffusion from the tip to the substrate is believed to be facilitated by the water meniscus that forms between the two [22, 23], hydrocarbon deposition without meniscus has also been reported [24]. In either case however the material deposition was established to be diffusion driven. The water meniscus is formed from residual water that is present on the surface of the sample and the tip under ambient conditions. As the tip is moved close to the surface, a capillary force acts on the water that is present and moves it towards the interface between the tip and the surface. This position (at the tip-surface interface) is the thermodynamically preferred position of the water in such a system and has been well studied [23, 25,

26]. Dip-pen lithography has advantages over other techniques as it can be used to print hard and soft materials, this makes it a useful technique in biology for depositing soft materials onto various substrate surfaces [27].

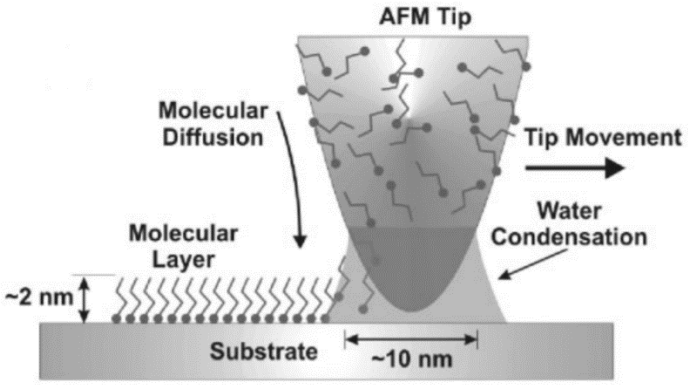

Figure 2.2: Schematic diagram depicting dip-pen nanolithography [17, 21]

2.3. Filaments: direct-write (DW) printing

Direct-write (DW) printing [28] uses a computer-controlled extrusion system as shown in Fig. 2.3A. The ink to be printed is extruded from a nozzle either pneumatically or using capillary action between the ink and the substrate; the ink forms a filament spanning from the nozzle to the substrate and the relative motion between the nozzle and the substrate can be used to obtain printed features. High-resolution (with μm or nm repeatability) positioning stages can be employed for moving either the substrate or the nozzle to facilitate the relative motion (Fig. 2.3B). Also, a collocated long-distance microscope is used to monitor and set the nozzle-substrate distance.

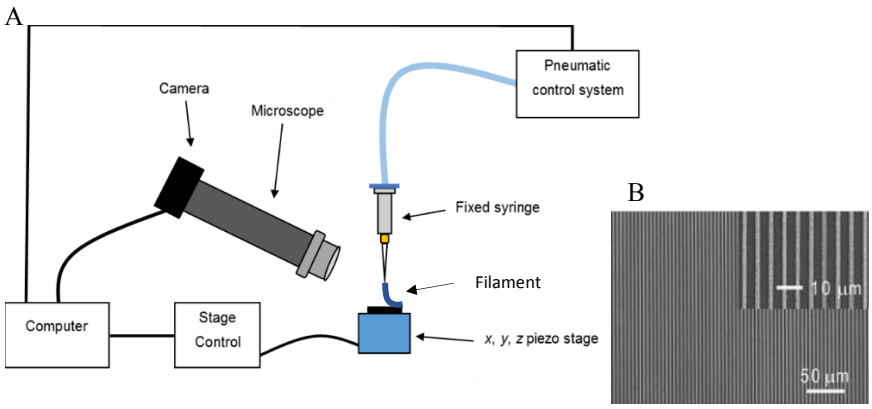

Figure 2.3: (A) Schematic of DW printing setup using custom-made nozzle with diameter controlled down to ~100 nm, and (B) an example of DW printed silver electrode array [29].

Many different types of inks have been shown to be printable at high-resolution with this type of setup such as colloidal suspensions, fugitive organic inks, hydrogels, sol-gels, polymers, polyelectrolytes and nanoparticle filled inks [29]. A big advantage of DW printing operations is that no temperature control system is needed when the inks are suitably formulated. Most of the inks can be deposited at room temperature, but some inks such as polyelectrolyte inks need a coagulation reservoir to enable 3D printing [30]. To achieve further stability of the printed structures, post-treatments are usually used, for example, thermal annealing or UV curing.

Print resolution in this case depends on nozzle size, nozzle and substrate wettability, ink rheology and evaporation characteristics (to be discussed in greater detail later) and the stability of the direct-write filament between the nozzle and the substrate. For Newtonian liquids, Plateau established that filaments with lengths less than their perimeter are stable in static conditions; under dynamic conditions, especially when the ink solvent is evaporating during the DW printing process, the filament stability is complicated [19, 31]. The evaporation of the solvents raises the concentration of solutes or dispersed phases with time, which should improve the stability of the filament [8]. However, too rapid evaporation can cause nozzle clogging. High solute or dispersant loading will increase filament stability; however, this will also raise the pressure drop across the nozzle. Thus, ink formulation requires careful control of its constituents [32].

2.4. Nozzle-less printing

One way to overcome the issue of inks clogging inside the nozzle during printing is to simply remove the printing nozzle altogether. This interesting approach in fact has been realized using a number of different techniques, each of which show varying, but exciting promise. In this section, we will highlight two key nozzle-less printing methods, explain the principles behind them and discuss how they have maintained high-resolution printing without requiring a microscale nozzle.

2.4.1. Pyroelectrohydrodynamic printing

This dispensing approach was introduced in the last decade and it uses a pyroelectrohydrodynamic dispenser to create attoliter liquid droplets without the use of nozzles [33].

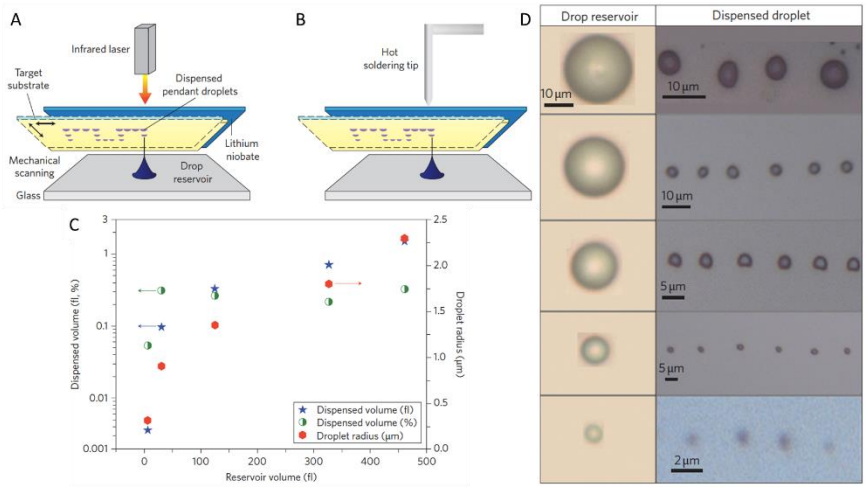

Figure 2.4: Pyroelectrohydrodynamic dispenser and exemplars. (A) and (B) are schematic illustrations of a pyroelectric printing approach which consists of two plates and a heat source (laser or hot tip of a conventional soldering iron) [34]. (C) shows the relation between the dispensed droplets and the drop reservoir in terms of volume and radius. (D) displays optical microscope images of different drop reservoirs and corresponding dispensed tiny droplets [33].

The system requires two plates (a target plate for droplet dispensing and a slab of pyroelectric material, such as lithium niobate) and a heat source (e.g. an infra-red (IR) laser or a hot soldering tip) as shown in Fig. 2.4A and B. Scanning the heat source over the lithium niobate substrate creates local pyroelectric forces, which deform the liquid (ink) meniscus locally akin to EHD printing. At sufficient thermal pulses, just as in EHD, micro or nanoscale droplets are formed and driven from the reservoir to the target plate. Various patterns can be achieved by moving the heat source to manipulate the shooting direction at different angles and locations [33, 34].

The size of print droplets could be reduced by decreasing the volume of the drop reservoir as shown in Fig. 2.4C, which indicates a positive correlation between their sizes. The optical microscope images (Fig. 2.4D) present the tiny droplets of oleic acid dispensed from drop reservoirs with various volumes and dimensions. The smallest dispensed droplets had volumes as low as 3.6 al and radii of 300 nm as can be found in Fig. 2.4C [33]. Overall, in terms of printing resolution, the printed droplets had sizes comparable to the electrohydrodynamic approach [35], which means that the pyroelectric approach also has the ability of high-resolution printing.

2.4.2. Laser-induced forward transfer (LIFT) printing

Another nozzle-less printing technique is laser-induced forward transfer (LIFT). This technique involves shining focused laser pulses at a surface to cause material ejection above the intended substrate. In this approach, shown schematically in Fig. 2.5A, focused laser pulses are directed towards a carrier surface held parallel to the

printing substrate. This suspended carrier is actually composed of multiple layers. In its simplest form, it has a transparent glass layer (carrier/support layer) and a thin film of the material to be printed (donor layer) coated over it [3]. When the laser pulse hits the surface, it propagates through the transparent carrier layer and is absorbed by the donor layer. Depending on the fluence of the laser pulse (i.e. energy input per pulse in $J\ m^{-2}$), the donor layer may melt or be vaporized [36]. The melting/vaporization causes a pressure change at the carrier layer-donor layer interface. This in turn forces the ejection of a liquid droplet of the donor material which falls to the substrate surface beneath [3]. When it reaches the substrate the droplet cools and solidifies. A fresh location of carrier/donor material is then positioned at the lasers focus and the substrate is moved to create the printing pattern.

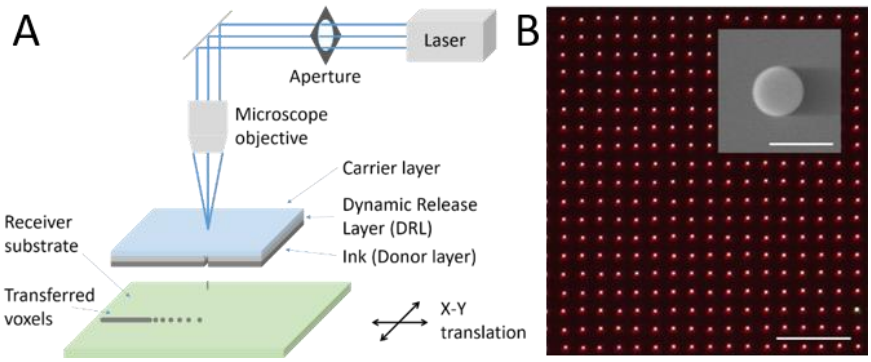

Figure 2.5: laser-induced forward transfer (LIFT). (A) shows a schematic of the printing setup and (B) is a printed amorphous silicon nanoparticle array (dark field optical microscope image), with scale bar of 20 μm and the inset showing an SEM image with 200 nm scale bar. Diameter of each nanoparticle is ~160 nm [37].

This two layer carrier/donor method has been shown to print a wide range of single element materials such as copper, gold, aluminium, tungsten and many more [38]. Fig. 2.5B shows an example of Si nanoparticle arrays printed using LIFT [37]. A limitation of the method is that the material undergoes a phase change as it is ejected. For many materials this phase change can detrimentally affect the properties of the printed material such as its electrical behavior, structure, homogeneity, chemical activity and biological activity [38]. To overcome this issue a different approach is taken, multi-layered donors. Instead of the donor layer directly absorbing the laser light an additional absorbing layer is sandwiched between the carrier and the donor layers. This layer is referred to as the dynamic release layer (DRL) [38]. The DRL then undergoes melting or vaporization when the laser pulse is absorbed, generating the pressure change required to eject the donor material. By selecting the appropriate DRL an even wider range of materials can be printed. Fluid materials containing biological cells can be printed by using a thick polymer DRL coated in a thin film of the fluid. When the laser pulse interacts with the DRL in this

case it causes plastic deformation which mechanically ejects the fluid onto the substrate (blister-actuated LIFT) [38].

For bi-layer LIFT systems, at fluences above threshold a thermally induced nozzle regime (TIN) can be reached [3]. At these fluence values the thermal diffusion length is less than the donor layer thickness. This prevents the donor material from being fully liquified. The liquified material travels from the carrier-donor interface to the ejection surface. When this wave of molten material reaches the ejection surface it breaks through and is ejected through a small quasi-nozzle [3]. Jetting can also occur in the TIN regime. At even higher fluences spraying is encountered [38].

2.5. Transfer printing

Basic principle of transfer printing is analogous to stamping, wherein a patterned stamp is wet by a suitably formulated ink, followed by a physical contact of the stamp with the substrate which allows a capillarity enabled transfer of the stamp pattern to the substrate. Using techniques such as photolithography, the features in the stamp can be manufactured with micro and nanoscale precision, which can be exploited to achieve high-resolution pattern transfer. A high-fidelity pattern transfer however requires careful control of the ink rheology, wettability and elastic properties of the stamp and the substrate [39]. Depending on the exact design of the stamp and the pattern transfer process, transfer printing can be of several different types (see Fig. 2.6), e.g., relief, intaglio, lithography and screen [18, 40].

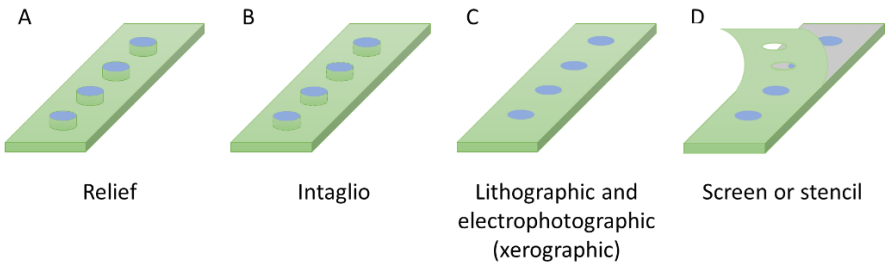

Figure 2.6: Diagram of the patterning elements (blue) with the ink (red) of major print techniques: (A) Relief printing, (B) intaglio printing, (C) lithographic printing and electrophotographic (xerographic) printing, (D) screen or stencil printing. Concept adopted from [40].

Relief transfer printing is based on a classical stamp composed of raised parts that make contact with the surface they are being pressed onto. The ink to be transferred (red colour in Fig. 2.6) is placed onto these raised areas and is transferred from the raised design to the substrate when the “stamp” is removed.

Intaglio transfer printing is the inverse of relief printing as the design of the “stamp” is such that the ink is in sunken wells instead of on raised parts. The wells can be filled and the substrate placed on top and the ink is transferred when the top surface is lifted off.

Lithographic transfer printing is similar to relief transfer printing but instead of physically raising areas to create contact patterns, a flat surface is treated so that only certain areas hold ink on them and in the other areas the ink does not stick. Then the same principle applies as before when this is pressed onto a surface the ink is transferred.

Screen transfer printing differs slightly from the previously described methods as it uses a stencil instead of a stamp. The stencil is applied to the surface to be printed on and then ink is applied on top of that. The ink then goes through gaps in the stencil so that the ink is only applied to the chosen areas on the printing surface. Then the stencil is removed and only the stencil pattern of ink remains.

High-resolution requires reducing the features sizes of the stamp or the stencil. However, by reducing the features sizes the durability of the stamps decreases as the contact between two hard surfaces applies a lot of pressure on them. A better technique at high-resolution is to create conformal stamps. A conformal stamp can be created by using a patterned elastomeric material as the printing layer [41]. When in contact with the substrate the conformal stamp macroscopically conforms to the shape of the substrate and microscopically adapts to the surface roughness leading to intimate contact [40]. Transfer printing has been exploited to demonstrate multi-layer and 3D structures [42] and, in combination, with directed self-assembly of block copolymers, has been demonstrated to achieve sub-10 nm resolution [43].

3. Fluid mechanics features

In this section, we will discuss some of the key fluidic features that influence fluidics assisted high-resolution 3D printing. We begin with ink properties by defining key rheological parameters. We then move on to substrate wetting. The next features we examine are nozzle properties, e.g., nozzle size and wettability and their role in the final print resolution. Finally, the section ends with dynamic effects such as evaporation and the features of drop impact on the substrate. In each case we will also discuss techniques to tune the print resolution and quality and/or overcome the limitations that these fluidic features introduce.

3.1. Ink rheology and pressure drop

Ink properties are critical to deciding the printing resolution and stability of printed structures. Here we will explore the rheological properties of ink such as viscosity and viscoelasticity along with discussing their role in controlling the pressure drop across the printing nozzle and stability of printed features.

Viscosity measures a fluid's resistance to deformation from an applied stress. Viscous resistance plays an important role in fluidics assisted high-resolution 3D printing, since all fluid flows are under stresses in shear and/or normal directions. Depending on whether the fluid viscosity is strain rate independent or dependent, fluids are categorized as Newtonian and non-Newtonian, respectively.

Non-Newtonian fluids can be further categorised as follows. Shear thickening liquids have a viscosity that increases with shear rate, shear thinning liquids have viscosity that decreases with shear rate, thixotropic liquids have a time dependent viscosity which decreases at a constant shear rate, rheopectic liquids have a time dependent viscosity which increases at a constant shear rate, Bingham plastics are fluids that display solid like properties at low stress and viscous characteristics at high stress and Herschel-Bulkley fluids have solid like behaviour at low shear rates and a shear dependent behaviour at higher shear rates [44, 45], etc.

In high-resolution 3D printing, non-Newtonian fluids are often encountered. Ahn *et al.* tuned the ink viscosity by varying moisture and nanoparticle content, and achieved an optimal range of viscosities for printed line spreading control as well as 3D printing features [29].

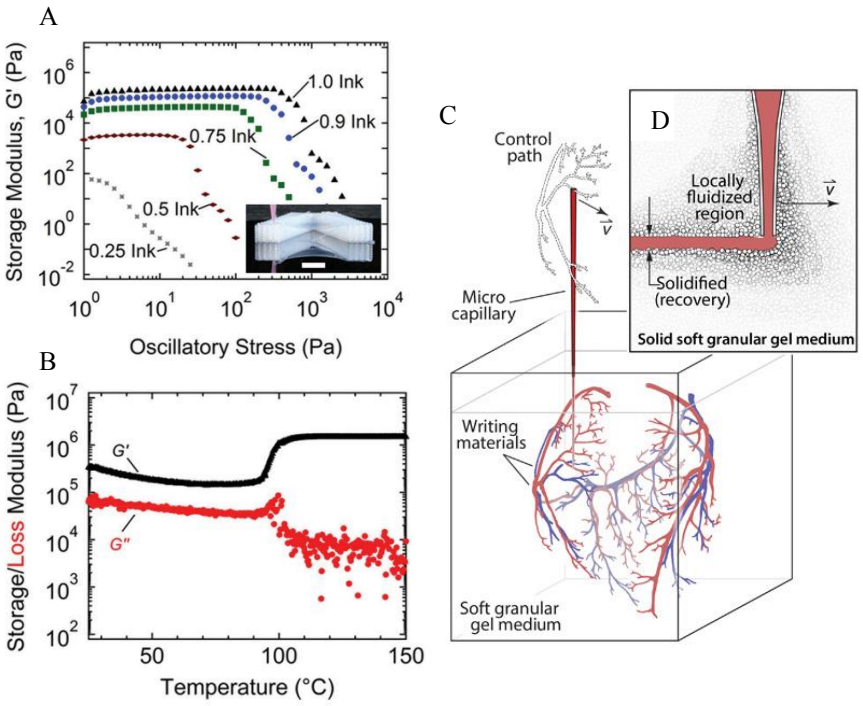

Figure 3.1: (A) Variation in the storage moduli versus oscillatory stress for varying dilutions of a silica-filled polydimethylsiloxane (PDMS) adhesive ink material. (B) temperature dependent variation of the ink storage and loss moduli indicating initiation of cross-linking at ~90°C [46]. (C) and (D) complex objects being printed in a granular gel for support by injecting material [47].

Recently, printing of softer materials has received wide-spread attraction for tissue engineering, bio-scaffolds, and flexible electronics applications. The behaviour of these materials can neither be characterised as a pure liquid with viscous dissipation nor as a pure solid with elastic properties. Their properties in fact reflect both elastic (solid-like) and viscous (liquid-like) characteristics. Thus, these materials are termed as viscoelastic materials. The dynamic modulus (G) is used to describe the rheology of such viscoelastic materials. The dynamic modulus relates the materials' dynamic stress and strain and can be expressed as

$$G = G' + iG'' \tag{3.1}$$

where i is square root of −1. Equation 3.1 essentially states that G can be separated into two components, the storage modulus (G') which captures the elastic properties and the loss modulus (G'') which characterises the viscous properties. Each of these moduli can be measured by subjecting the material to an oscillatory shear deformation [48] and measuring the resulting dynamic stress and strain parameters using a rheometer as:

$$G' = \frac{\sigma_0}{\varepsilon_0} cos\,\delta\,;\; G'' = \frac{\sigma_0}{\varepsilon_0} sin\,\delta \tag{3.2}$$

where σ_0 and ε_0 are respectively the stress and strain amplitudes recorded by the rheometer, and δ is phase difference between these two moduli.

A high value of G' facilitates stability of printed 3D structures [8]. Fig. 3.1A shows the results of a study designed to examine how dilution of an ink influences its storage modulus. The study looked at an adhesive ink of silica-filled polydimethylsiloxane (PDMS) [46]. Dilution of the ink was achieved by adding unfilled PDMS to the silica-filled PDMS. The decrease in the storage modulus can be seen to occur at lower oscillatory stresses as the dilution increases. Above 50% dilution (0.5 Ink) the storage modulus decreases immediately. This indicates that the storage modulus and the ink viscosity are too low for stable 3D printing filaments to form.

Fig. 3.1B shows how the storage and loss moduli vary with temperature. The sharp change at approximately 90 °C signifies thermal curing. By knowing at what temperature this change occurs we can determine the minimum temperature required to thermally anneal printed structures.

Printing 3D structures of soft materials and gels with low G' values poses a challenge. Recent advances have included a number of workarounds such as exploiting a sacrificial sugar layer to be dissolved away [49], or printing in a bed of gel-like material which offers structural support [47, 50]. Fig. 3.1C and D show an example of using granular gel as a 3D writing medium which has yield stress and shear thinning properties. The shear thinning property facilitated easy movement of the printing nozzle through the gel, whereas after printing the yield stress helped sustain the soft printed features (see Fig. 3.1D). The approach enabled soft materials with elastic modulus less than 100 kPa to be printed [50].

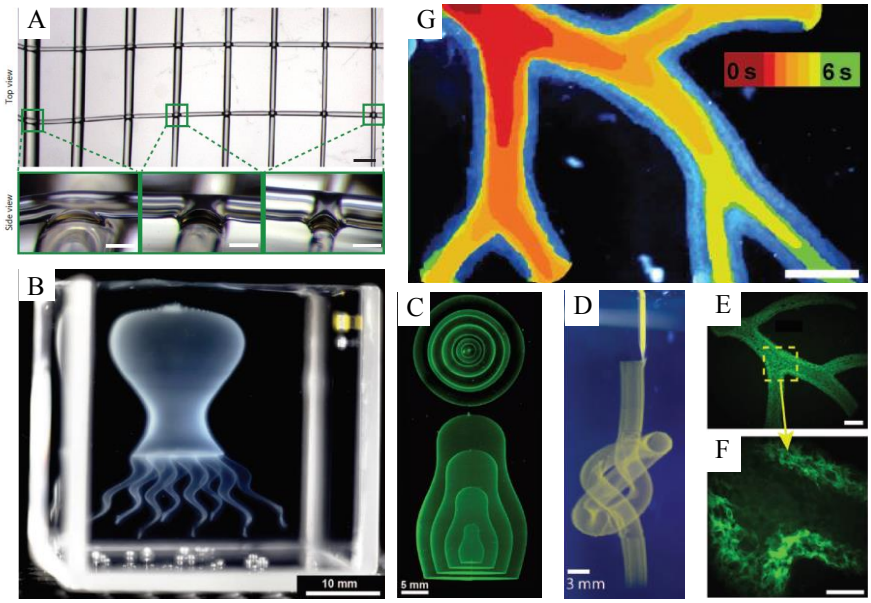

Figure 3.2: (A) printed carbohydrate glass which could be used as support for cell culturing [49].

(B)thin shell octopus model printed in a granular gel (Bhattacharjee *et al.*, 2015). (C) and (D) complex structures printed in a granular gel, Russian dolls and a knot [47]. (E) and (F) printed arterial tree with a hollow lumen and bifurcations. (G) time lapse of dye perfusing through arterial tree demonstrating flow through the lumen and not the walls [50].

Some specific examples of structures printed using support gel materials are displayed in Fig. 3.2. Fig. 3.2A shows some of the printed sugar glass structures ready to have cells cultured around them. This technique uses the printed sugar glass as a sacrificial medium to create the desired networks. This method showed how sacrificial material could be used to overcome structuring problems of soft materials and used to grow bioscaffolds. Such an ability to create vascular networks in engineered tissue constructs would prevent cell necrosis (death) inside the construct. To create perfusable vasculature an idea was brought forward to print sugar glass networks, grow the cells around them and then dissolve away the sugar glass to create the vasculature structure [49].

Fig. 3.2B- D show some examples of the types of complex structures that can be printed using a granular gel as support structure. The intricacies achieved clearly demonstrate the potential of the methodology. Fig. 3.2B shows a thin-shell model octopus made from multiple connected hydrogel parts with a complex, stable surface. Fig. 3.2C shows printed Russian dolls, demonstrating the ability to encapsulate structures within one another. Fig. 3.2D shows a continuous knot written with an aqueous fluorescent microsphere suspension inside the aqueous gel.

Another technique has also been used to create perfusable vasculature, this time directly printing the vasculature network in a supporting gel [50] similar to the granular gel support printing described above. Fig. 3.2E and F show a section of the printed vasculature. These figures show the hollow lumen achieved, as well as the multiple bifurcations while maintaining a vessel wall thickness of less than 1 mm [50]. Fig. 3.2G shows a time lapse image of dye perfusing through the vasculature, demonstrating that the flow is through the lumen not the walls.

An important parameter which affects the printing process is pressure drop through the printing nozzles. To a first approximation the pressure drop through a nozzle can be understood by considering the nozzle to be a uniform diameter capillary. With this approximation, the flow rate and pressure drop relationship for a power law fluid (a common ink type) can be written as [4]:

$$Q = \frac{n\pi}{3n+1}\left(\frac{1}{2\mu}\frac{\Delta p}{l}\right)^{1/n} R^{3+1/n} \tag{3.3}$$

where Q is fluid flow rate, μ is the dynamic viscosity, R is the inner radius of the capillary, and Δp the pressure drop over a length l. The result for a Newtonian fluid (Poiseuille relationship), can be obtained by substituting n equal to 1. Clearly, for the same flow rate, the increase in pressure drop with reduction in capillary radius is very high. In fact, in the Newtonian case, with a reduction in radius by a factor of two, the pressure drop rises by a factor of 16, thereby clearly highlighting the challenges of high-resolution printing as discussed above.

3.2. Substrate Wetting

Substrate wetting by ink has a direct influence on the resolution and the adhesion of the printed structures. A droplet placed on a substrate offers first insight into the wettability and takes a form dependent on three different surface energies: interfacial tensions between liquid-gas (γ_{LG}), solid-liquid (γ_{SL}) and solid-gas (γ_{SG}). The latter is surface energy of the solid and γ_{LG} is the surface tension of the liquid, also used earlier without the subscript. The competition of these three different surface energies decides the shape a droplet assumes on the substrate. In the so called partially-wetting regime on a smooth, homogeneous substrate, the droplet takes the form of a spherical cap (see Fig. 3.3A) with an angle at the periphery. This angle is formed at the contact line, where the three interfaces meet and the interfacial tensions are in balance. For a smooth spherical cap shape the contact line is circular. The angle θ is referred as Young's contact angle. "Real" substrates have minimal roughness and also tend to have heterogeneity. This affects the surface wetting and results in different angles for an advancing and receding liquid interface. The advancing and receding angles θ_A and θ_R can be measured by gradually increasing and decreasing the volume of a liquid droplet on the substrate and measuring the resulting contact angles (see Fig. 3.3B and C). Difference in θ_A and θ_R is referred to as contact angle hysteresis and it plays an important role in the printing process [5]. For example, for a large hysteresis a printed droplet can become pinned on the substrate and evaporation of the solvent can lead to a non-uniformity of the deposit (see 'coffee ring' effect discussed below). Surface treatment techniques such as roughening, plasma treatment, surface functionalisation with various chemicals, etc. can be used to form the monolayer on the substrate and alter the contact angle and thereby the printing resolution (see Fig. 3.3D-F). Fig. 3.3D shows oxygen plasma treated acrylic, Fig. 3.3E untreated acrylic and Fig. 3.3F shows a droplet on acrylic spray coated with a superhydrophobic coating [51]. Such wettability manipulation techniques are frequently employed to alter the surface adhesion and/or printing resolution.

The surface energies mentioned above are directly related to the work of adhesion (W_{ad}), which is a measure of the liquid adhesion with the substrate. The work of adhesion is essentially the energy (per unit area) required to separate a liquid from the solid it is lying on and can be shown to be [52]

$$W_{ad} = \gamma_{LG}(1 + cos\theta) \tag{3.4}$$

The Equation 3.4 clearly indicates that the existence of advancing and receding contact angles correspond to a hysteresis in the energy 'spent' to destroy a liquid-solid interface by separating them and the energy 'obtained' by forming them. This can be understood by replacing the contact angle in Equation 3.4 by θ_A and θ_R, respectively. Generally, for every real substrate θ_R is smaller than θ_A, this amounts to a positive energy penalty in the removal of a liquid, relative to forming the interface by advancing the interface on the substrate. In other words, a high contact angle hysteresis may in fact be advantageous for promoting adhesion of the printed inks

and features on the substrate. Additionally, the hysteresis can also help by adding additional stability to liquid filaments and liquid bridges in direct-write and dip-pen printing techniques mentioned above.

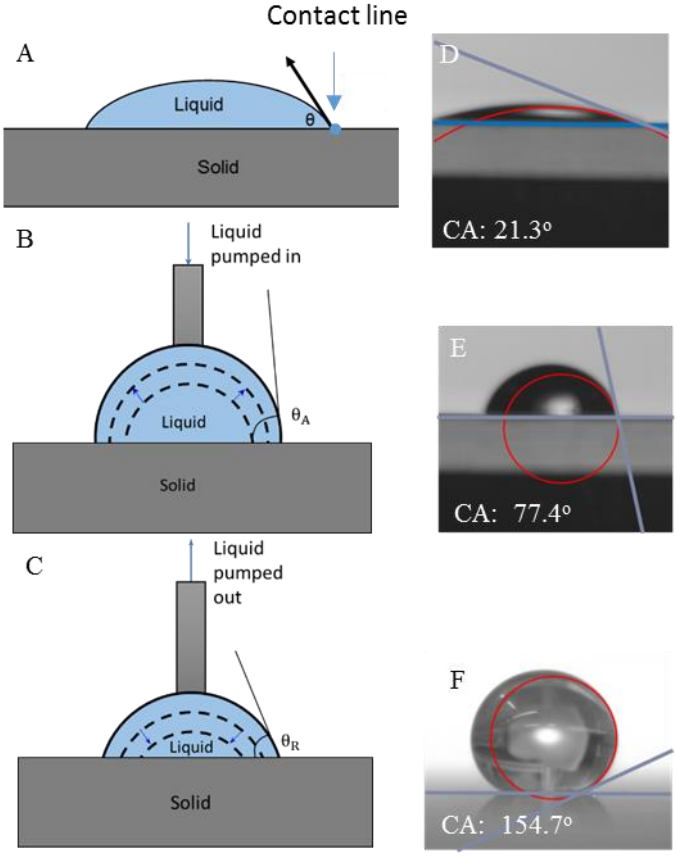

Figure 3.3: (A) Contact angle of a liquid droplet on a solid substrate. Measurement of (B) advancing and (C) receding contact angles. And contact angle measurement on (D) plasma treated surface, (E) untreated surface, and (F) hydrophobic surface.

3.3. Nozzle properties

For printing techniques employing nozzles, nozzle properties obviously play an important role. Finer nozzles are typically prepared by pulling glass capillaries using a micropipette puller followed by coating them with metal film, if required. Some direct-write approaches using modified AFM tips, rely on photolithography and etching processes to manufacture hollow AFM tips [53]. Nozzle size and wettability are the two most important nozzle properties influencing printing and are discussed sequentially below.

3.3.1. Nozzle size

The resolution of printed features is directly related to the diameter of the printing nozzle. As mentioned above, the DW printing technique uses a back pressure to extrude the ink through the printing nozzle to form a filament. The size of the filament is closely dependent on the nozzle diameter, with the wettability and the ink evaporation obviously also having an influence.

In EHD printing, the resolution is related to the size of the droplet. Typically, the droplets and e-jets are an order magnitude smaller than the nozzle (meniscus) size. This is an advantage of EHD printing as the clogging issues increase with reduction in nozzle diameter (see discussion on ink evaporation, discussed below). To obtain micro/nanoscale droplets, the applied voltage needs to be controlled precisely.

3.3.2. Nozzle wetting

Nozzle wetting has an important role in deciding the size of drops and filaments. A careful control of nozzle wettability can add to stability of printing and/or also help control the printing resolution. Fig. 3.4 shows the comparison results for nozzle wettability effects [54]. From left to right, the form of the liquid meniscus is shown on hydrophilic, hydrophobic and superhydrophobic nozzles, as observed by Dong *et al.*[54]. For the hydrophilic nozzle, water overflows out of the nozzle, across to the outer surface and up the outer wall. For the hydrophobic nozzle, a pendulous droplet was pinned at the outer edge of the nozzle. For the superhydrophobic nozzle, the droplet did not move past the inner edge of the nozzle-tip surface due to the strong restrictions caused by the superhydrophobic edge effect.

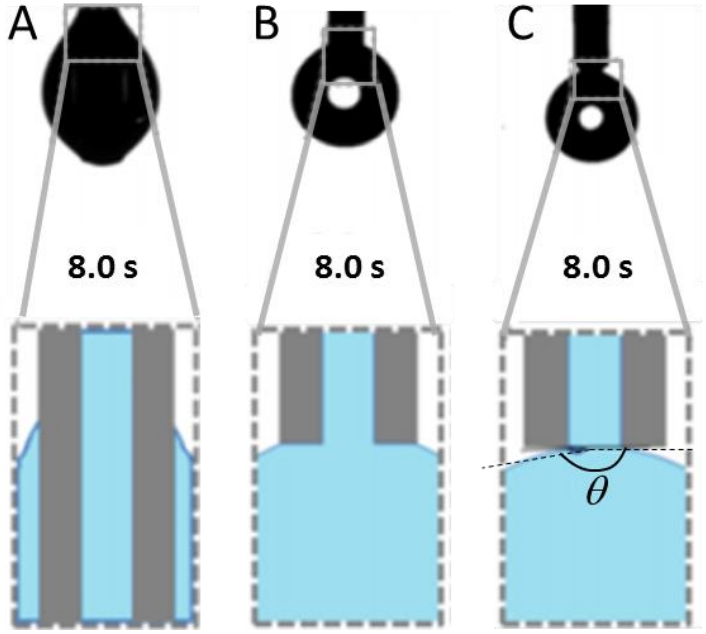

Figure 3.4: Correlation between the size of dripping droplets and the wetting property of the nozzles, highlighting a clear expected role of nozzle wettability on printing resolution. Photographs of the dripping droplets from nozzles with different wettability on the top, with the schematics of the menisci and contact line positions illustrated at the bottom. From left to right is (A) hydrophilic nozzle, (B) hydrophobic nozzle and (C) superhydrophobic nozzle [54].

The following gravity and capillary force balance can predict the volume of the dripping droplet from the nozzle

$$V = \frac{\pi \gamma D \sin\theta}{\rho g} \tag{3.5}$$

where V is the volume of a droplet, D is diameter of the droplet contact line at the nozzle, θ is the liquid detaching contact angle and γ and ρ are surface tension and ink density respectively.

The tip of the nozzle can be thought of as a surface with a contact angle and contact line. In the case of the hydrophilic nozzle, the contact line has moved up away from the tip and is around the outer diameter of the nozzle (Fig. 3.4A). The contact angle is more obvious for the hydrophobic and superhydrophobic nozzles as the contact lines are pinned at the outer and inner diameter edges respectively. The contact angle is measured as described above at the point where the liquid, solid and gas phases met. As the capillary force acts on the droplet at a diagonal we use geometrical analysis to calculate the vertical component resisting the gravitational force, resulting in Equation 3.5. Due to the increasing contact angle as we progress towards superhydrophobic nozzles, the attachment area for the droplet is getting smaller. For a superhydrophobic nozzle the contact diameter matched with nozzle

inner diameter D_i, thereby leading to smallest size of the dripping droplet (down to picoliter volumes). This means that less mass can be supported at the tip by the capillary force resulting in smaller droplet volumes and hence smaller droplet sizes. As droplet size and meniscus location are closely related to printing resolution, this discussion clearly shows that we can increase resolution in fluidic assisted printing by carefully controlling the surface properties of the printing nozzles used.

3.4. Dynamic effects

The printing process by its nature is dynamic and is thus influenced by a number of key related features such as liquid(ink)-solid(substrate) dynamic impact, ink evaporation etc. In fluidics assisted printing techniques these features not only influence the quality and resolution but in fact can be exploited to expand the capability of printing techniques. For example, tuning evaporation rate can help use droplet based printing technique to print 3D structures or controlling the in situ evaporation and changes in viscoelasticity of inks can enable printing of self-supporting 3D structures.

Controlling evaporation is important to ensure stability of the printing process itself. Evaporation will influence many aspects of fluidics assisted high-resolution printing. Starting in the nozzle, if the evaporation rate is too high then the solvent will evaporate out and the ink will solidify before it is deposited onto its intended surface. Assuming that the evaporation rate is not too high and the ink can be successfully extruded, the evaporation rate still plays a key role even once the ink is deposited onto its intended surface. The evaporation will influence factors such as the spreading on the surface, the drying/potential 3D structuring of the pattern and the homogeneity of the cured ink in the printed structure. Features of evaporation and its effects can be understood by analysing the relevant time scales.

On most real surfaces with contact angle hysteresis, evaporation of a liquid drop occurs with its contact line pinned. For good substrate adhesion (see the substrate wettability section above), a low contact angle is desirable. The time scale of evaporation for a droplet with pinned contact lines in the regime of low contact angles can be written as [6]:

$$\tau_{evap} = \pi {d_c}^2 \frac{\theta_0 \rho_l RT}{64 D_l M_l \Delta p} \tag{3.6}$$

Where d_c is the pinned contact diameter, ρ_l is the liquid density, M_l is the molecular weight, D_l is the diffusion coefficient of the liquid vapour, T is the temperature of the liquid vapour, Δp is the partial pressure difference, R is the gas constant and θ_0 is a low contact angle.

The partial pressure difference is calculated between the pressure at the liquid gas interface and the pressure at infinity (very far from the interface). This difference is the driving potential for evaporation.

Therefore, for 3D printing, to build up consecutive layers the time between printing each layer must be greater than the time of evaporation so that the solvent can evaporate out and the ink solidifies. In some printing setups, the ink is not solidified via solvent evaporation and other methods are used such as a chemical reaction or cooling through a transition temperature.

As stated previously we are looking at evaporation in a regime where the contact line is pinned. In this regime, the evaporation rate is greater at the contact line than at the centre of the drop. The ensuing non-uniform vapour flux causes the ink in the middle of droplet to flow towards the contact line. Since the evaporation rate is greater at the contact line, the solvent is removed and any particles it was carrying get deposited there. Therefore, there is an uneven deposition of particles around the contact line. This has come to be known as the "coffee ring" effect [55], because the same mechanism decides the ring like patterns forming when a drop of coffee dries out on a table or a floor. When printing structures this is an undesirable effect so efforts have been made to try and overcome it.

In addition to the evaporation time (τ_{evap}) mentioned above, we must consider the time scale for particle diffusion (τ_{part}) through the ink in order to determine the likelihood of coffee ring formation. The idea essentially is that, if $\tau_{evap} < \tau_{part}$, then the particles would not have time to diffuse to the edges (contact line) in order to see the coffee ring formation, essentially freezing them in their original homogeneous dispersion with very quick evaporation. This idea can be taken further as if there is continuous evaporation of the carrier solvent then the contact angle of the droplet can be reduced to less than the critical receding angle limit (θ_{rec}). Below this θ_{rec}, the contact line is no longer pinned and a coffee ring is unable to form. Therefore, the updated evaporation time can be expressed as:

$$\tau_{evap} = \pi d^2 \frac{(\theta - \theta_{rec})\, \rho_l RT}{64 D_l M_l \Delta p} \tag{3.7}$$

τ_{part} can be calculated by following the Einstein–Smoluchowski analysis of Brownian motion [56].

$$\tau_{part} = \frac{\bar{L}^2}{2D_p} \tag{3.8}$$

where D_p is the diffusion coefficient and $\bar{L}$ is the average separation between particles, which naturally depends on particle size and volume fraction.

The diffusion coefficient is given by the Stokes-Einstein relation [57].

$$D_p = {k_B T}\Big/{3\pi\mu d_p} \tag{3.9}$$

Where k_B is the Boltzmann constant, T is the temperature, μ is the dynamic viscosity and d_p is the particle diameter.

The average particle separation can be calculated as:

$$\bar{L} = \left(\sqrt[3]{\pi/(6\phi)} - 1 \right) d_p \tag{3.10}$$

where ϕ is the particle volume fraction and d_p is the particle diameter [58].

A further analysis on evaporation time, including hydrophobic surfaces, was carried out by McHale *et al*. [59]. Hydrophobic surfaces are those that have a low contact angle hysteresis so droplets that land on them find it very difficult to adhere and simple roll off the surface. With these types of surface, the contact line can move and therefore the droplet needs to keep a constant contact angle to evaporate. The result of this analysis is shown below.

$$\tau_{evap} = d_c^2 \frac{\rho_l RT}{16 D_l M_l \Delta p} \frac{(1-\cos\theta)(2+\cos\theta)}{sin^2\theta} \tag{3.11}$$

where d_c is the contact diameter. For all given equations for evaporation time (Equations 3.7, 3.8 and 3.11) the time scales with the contact diameter squared. For high-resolution printing, this means that as we reduce the contact diameter to improve the resolution we also increase the evaporation rate. If we decrease the contact diameter (and hence resolution) by one order of magnitude the evaporation time speeds up by two orders of magnitude. This must be kept in mind when designing inks for use in high-resolution fluidic assisted printing.

Given the undesirability of coffee ring like deposits, a number of strategies have been developed to avoid it (Fig. 3.5). Shen *et al.* [57]first showed that coffee rings can be avoided by simply going to smaller droplets. This can be understood as follows. From the above discussion, by equating the expressions for τ_{evap} and τ_{part}, we can determine the critical droplet size (contact diameter) d_c to prevent coffee ring formation. In Fig. 3.5A, the "large" droplet on the right shows coffee ring formation, whereas the small droplet on left (with size below d_c) shows particle deposition throughout the droplet base, overcoming the coffee ring problem. This is an advantage for high-resolution printing. Note that in constant contact angle mode of evaporation, the contact line moves and thus the deposit is uniform to start with. Fig. 3.5B shows exploitation of Marangoni flow to overcome the coffee ring problem as first proposed by Hu and Larson [60]. Non-uniform evaporation of the pinned droplet causes a temperature gradient at the droplet-air interface, which can lead to a Marangoni flow, which can overcome the capillary flow involved in coffee ring formation and thus help avoid coffee ring formation. As another strategy, Yunker *et al.* [61] showed that coffee ring formation can also be avoided in suspensions of high aspect ratio particles such as ellipsoids. The reason was that once ellipsoidal particles reached the droplet-air interface, the long-ranged capillary interaction between the particles increased by two orders of magnitude and thus the particles were effectively locked in place, thereby forming a uniform deposit after solvent evaporation, unlike spherical particles where the capillary interactions were weaker (see Fig. 3.5D). Interestingly, they also showed that by mixing a small amount of high aspect ratio ellipsoidal particles into a spherical particle suspension this lead to a near uniform deposit formation. These strategies are naturally of great practical importance to high-resolution printing.

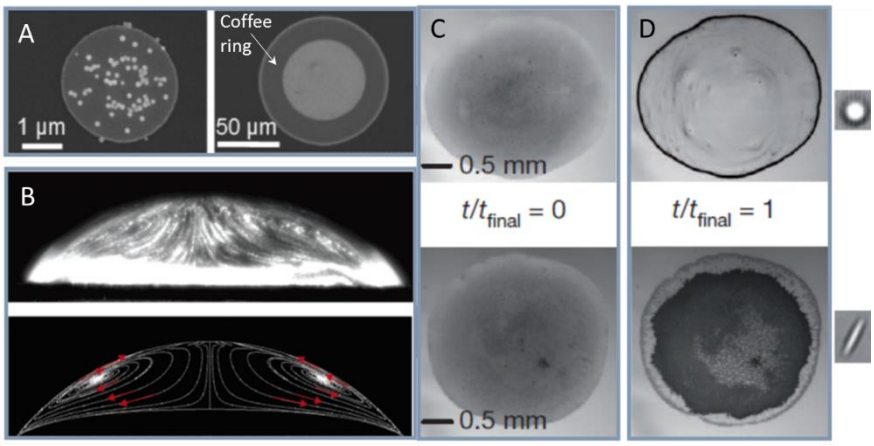

Figure 3.5: Coffee ring effect and its amelioration. (A) shows how the coffee ring effect (visible on the right) can be minimised by reducing the size of the droplet from 100 µm to 1 µm [57]. (B) shows Marangoni vortices in an octane droplet [60]. (C) shows the initial homogeneous dispersion of spherical particles (top) and elliptical particles (bottom) and (D) shows how the shape of the particles alters the trying patterns of the droplets over time and how elliptical particles prevent coffee ring formation [61].

The next dynamic feature is related to the dynamic impact of ink drops on the substrate. The exact form and dynamics of the impacting drops has been studied for a variety of different applications and its exact features depend on a number of physical parameters and non-dimensional numbers. These numbers are based on physical properties of the ink and can be used to describe drop impact and dynamics. The key non-dimensional numbers are the Reynolds (*Re*), Weber (*We*), Ohnesorge (*Oh*) and Bond numbers [62]. The Reynolds number is used to indicate whether a flow is steady or turbulent and is defined as:

$$Re = \frac{v\rho a}{\mu} \tag{3.12}$$

where v is the velocity, ρ is the density of the ink, a is the characteristic length and μ is the dynamic viscosity [62].

The Weber number is used to analyse the relative importance of inertia and capillary forces, and is defined as:

$$We = \frac{v^2\rho a}{\gamma} \tag{3.13}$$

where v is the velocity, ρ is the density of the ink, a is the characteristic length and γ is the surface tension of the ink [62]. It determines the features of drop shapes during and after impact.

The Ohnesorge number is the ratio of internal viscosity dissipation to the surface energy[63] and is defined as:

$$Oh = \frac{\sqrt{We}}{Re} = \frac{\mu}{(\gamma \rho a)^{\frac{1}{2}}} \tag{3.14}$$

The Bond number (*Bo*) captures relative importance of gravity to surface tension and can be expressed as:

$$Bo = \frac{\rho g a^2}{\gamma} \tag{3.15}$$

where ρ is the density of the ink, g is the acceleration of gravity, a is the characteristic length and γ is the surface tension of the ink [62].

For the densities of inks usually used in the printing setups described above (~1000 $kg\ m^{-3}$) and their surface energies (~0.1 $J\ m^{-2}$), by plugging in the length scale as 10 μm or lower, we can immediately see that in high-resolution printing the Bond number is far less than 1 ($Bo \ll 1$). This means that gravitational forces can be neglected, leaving inertial and capillary forces as dominant [62].

For low *We* (typical of high-resolution printing) droplets falling onto a solid surface the impact can be divided into two regimes: impact driven and capillary driven [64]. In the impact driven regime inertial forces dominate and in the capillary driven regime the initial velocity of the droplet is unimportant and a change in behaviour occurs at a critical value of *We*.

The *Oh* gives a measure of the force that resists droplet spreading [64].

Fig. 3.6 presents a schematic capturing the temporal evolution of drop shapes under different impact conditions. The time scale can be analysed using the following scaling

$$t^* = t(v/d_0) \tag{3.16}$$

where t is the time, v the drop impact speed and d_0 the droplet diameter [62].

The initial stage of the impact is purely kinematic and is short lived, $t^* = 0.1$ (approximately equivalent to < 1 μs). After the impact, there is a point of maximum spreading, when all the impact kinetic energy converts into surface energy; the viscous effects are negligible in this inertia dominant phase. Following this the droplet shows recoil and/or oscillations. These oscillations can be damped by viscous forces. At this stage, depending on the surface energy of the liquid (ink), the substrate and the air interfacial energies, surface tension (capillary) dominated gentle spreading can take over. For $t^* \approx 10$ to 100, the capillary force entirely dominates. When t^* exceeds a value of about 1000, the spreading is essentially at equilibrium and stops. If present, this final stage spreading is very important to fluidic printing as it can affect the print resolution.

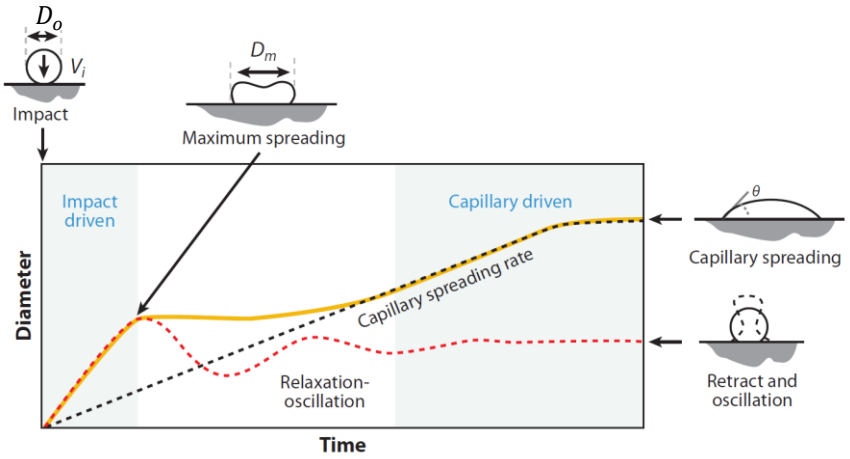

Figure 3.6: Schematic illustration of the sequence of events that occurs after droplet impact on a substrate. Initial impact is followed by a series of damped oscillations before capillary-driven flow occurs. θ is the contact angle, d_0 is the initial droplet diameter, Dm is the maximum radius to which a droplet spreads during impact, and V_i is the droplet velocity at impact [62].

At high impact speed, there is a danger of droplet splashing which can adversely affect the print resolution. To avoid splashing the following must hold [65]

$$We^{1/2}\, Re^{1/4} > f(R) \tag{3.17}$$

where $f(R)$ is a function of surface roughness only. This relationship has been explored by a number of authors, and for flat, smooth surfaces $f(R) \approx 50$ [65].

4. Exemplar demonstrations of high-resolution printing

In this section we present a number of salient examples of devices printed using various fluidics assisted, high-resolution 3D printing techniques. In addition to the techniques mentioned above, examples of hybrid printing techniques employing more than one basic printing principle are also presented.

4.1. Direct-write printing

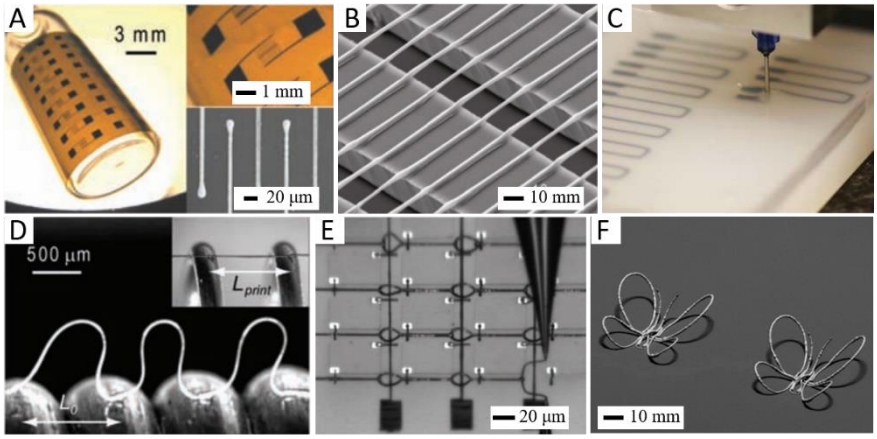

Figure 4.1: Exemplars of direct-write printing demonstrations. (A) and (B) are 2D structures with possible sensing applications, (A) shows silver microelectrodes printed on a flexible polyimide substrate and (B) demonstrates how Sn-doped indium oxide can be printed to span gaps [29, 66]. (C) shows an embedded printing process inside a reservoir filled with an elastomeric material; post-printing the printed filler material and the elastomeric matrix were cured to obtain flexible sensors [67]. (D) and (E) are printed arches for different applications. (F) are butterfly structures printed by in situ curing of direct-write silver filament to realise a 3D printing capability [68].

Direct-write printing has seen an increase in the diversity of materials being formulated as printable inks. As more and more materials become available to this printing process, it opens the door to a wide array of novel applications. Ahn *et al.* developed inks for different microelectrodes and metallic structures as shown in Fig. 4.1A and B. In Fig. 4.1A, silver microelectrodes were patterned onto a flexible polyimide substrate and also used as a strain gauge [29]. Fig. 4.1B shows microelectrodes so small that they are transparent to the naked eye. These microelectrodes have been printed using silver and Sn-doped indium oxide (ITO – a widely used, electrically conductive material, in optoelectronics) and demonstrate the stability of the structures by printing to span relatively wide gaps [66].

Stable 3D structures require sufficient storage modulus (G'). A number of methods have been developed to overcome the requirement of a high G' value, such as printing in a reservoir of supporting medium and using lasers and UV light to cure

the structure during the printing process. These techniques allow inks that would be unable to form 3D structures, due to low viscoelasticity properties, to achieve 3D structures. Fig. 4.1C shows a printing process, also known as embedded 3D printing (e-3DP), used to fabricate strain sensors inside a highly conformal elastomeric matrix [67].

Ahn *et al*. demonstrated how direct-write printing can be expanded to additional dimensions. By increasing the solid content of their inks they were able to achieve a higher value of G' which as discussed previously enables self-supporting structures. Fig. 4.1D and E shows printed arches Fig. 4.1D displays the flexibility of the silver arches by printing a line along a stretched spring. As the spring relaxes back to its equilibrium the silver line flexes and stretches with the spring resulting in the pattern shown. Fig. 4.1E demonstrates structural stability as arches of silver can be printed on a gallium arsenide–base to span across perpendicularly orientated wires [29]. Fig. 4.1G shows structures printed using a photonic annealing method applied during printing. The butterfly in Fig. 4.1G was printed using a laser to achieve point annealing immediately after extrusion form the nozzle[68]. Along similar lines, Lebel *et al.* manufactured helix structures by using UV light to anneal small areas after extrusion[69].

4.2. EHD printing

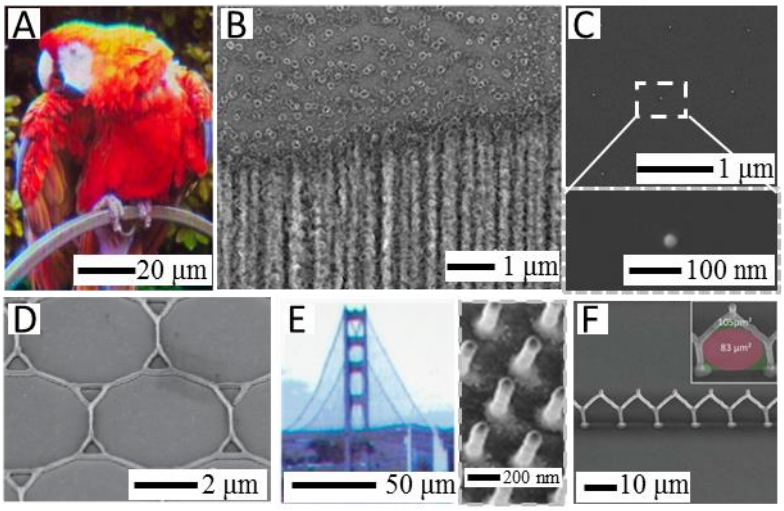

Figure 4.2: Exemplars of electrohydrodynamic (EHD) printing. (A) and (B) show two different magnifications of the same printing pattern, showing full spectrum colour 2D printing using a quantum dot suspension as ink; (B) is SEM image zooming near the parrot's eye. [70]. (C) top image shows an array of gold nanoparticles printed using inverse block copolymer micellar inks seeded with a gold salt, bottom image shows a zoom in to one gold nanoparticle[71] (D) are gold grid transparent electrodes [72]. (E) left image comprises of printed columns arranged to

recreate the image of a bridge, the right image shows a zoom in showing the columns [73]. The nanocomposite columns absorb light and help tune the colour of absorption spectra. (F) is a 3D printed archway structure used to study interstitial migration of cancer cells[74].

The versatility of EHD printing has been demonstrated through a large variety of features and devices. Fig. 4.2A and B shows how high resolution EHD printing can be used to print 2D patterns of red, blue and green quantum dots in order to create very high-resolution, full spectrum colour images. Fig. 4.2A shows the full picture which measures only 94 μm x 125 μm (about the same as the cross section of a human hair!). Fig. 4.2B shows the transition from the background to the printed area of some of the parrot's feathers.

Fig. 4.2C top shows an array of gold nanoparticles printed using an inverse micellar block copolymer ink seeded with gold salt; the image in Fig. 4.2C bottom shows an individual nanoparticle from the array. Post-printed copolymer-gold salt dots were plasma treated to obtain site specific deposition of the gold nanoparticles. Fig. 4.2D shows examples of 2.5D printing. Though this type of printing is out of plane, it is not fully-fledged 3D printing. Instead we refer to it as two and a half dimension (2.5D) printing, meaning that it is an out of plane extension of a 2D profile. Here we see gold electrodes composed of multi-pass EHD printing. These printed structures are so small that they are transparent to the naked eye. The electrical properties of these structures, combined with their small size, allows for transparent electronics to be created which could have many potential applications for devices such as touchscreens[72].

By controlling the drop size and ink evaporation, EHD can readily enable out of plane and 3D structures: Fig. 4.2E shows examples of this type, comprising an array of gold nanocomposite pillars. By carefully controlling the pillar heights, different levels of optical absorption in the visible range were achieved. Spanning from complete absorption to complete reflection the image of a bridge was successfully recreated [73].

Fig. 4.2F demonstrates the ability to create fully 3D structure with EHD. Printed archway structures are shown which were built up by carefully controlling droplet deposition to create multiple layers and patterns resulting in a 3D microstructure. Structures such as these were used to create micropores for interstitial migration of cancer cells [74] and to study high frequency data transfer induction [75].

4.3. Hybrid techniques

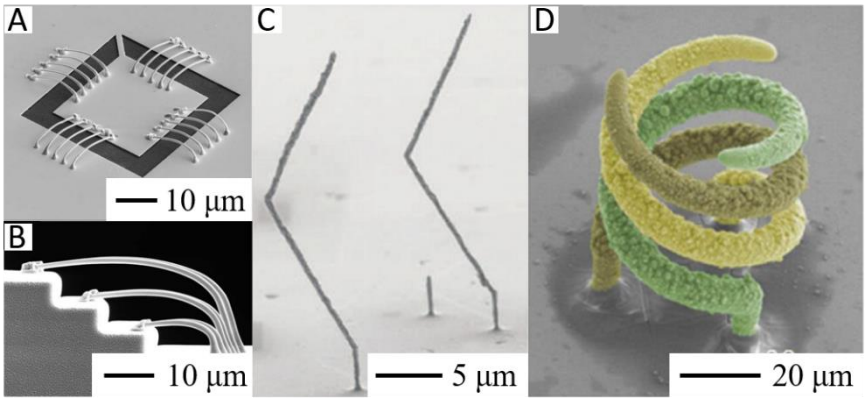

Figure 4.3: Exemplars of hybrid printing, where elements of direct-write and EHD printing are combined. SEM images showing (A) 20 electrodeposited interconnects with submicrometer diameters fanning out from a central pad with an area of 50 mm × 50 mm and (B) multilayered interconnection over three steps of 5 µm each in height. [76]. (C) Two zigzag structures fabricated by a dual-channel nanopipette [77]. (D) A triple helix, demonstrating the capability to fabricate intertwined shapes thanks to the layer-by-layer approach. The individual helices are colored for better distinction [53]. (A) and (B) printed using so called meniscus confined electroplating and (C) and (D) printed using in situ electroplating using dispensed ions in liquid. The imposed electric field is engendering electroplating here and the wetting or pneumatically enabled forcing of the ink enables 3D printing as in direct-write printing [53].

As high-resolution printing technologies advance, hybrid methods are beginning to emerge, which combine principles and techniques from different printing approaches to create unique techniques with specific advantages. We will focus on hybrid techniques which combine aspects of direct-write printing and EHD printing. One of the earliest hybrid techniques is meniscus-confined electroplating [76]. Standard electroplating is a surface reaction and in this technique the high-resolution is achieved by restricting the areas where the electroplating occurs using a liquid meniscus [3]. Meniscus-confined electroplating combines nozzle flow and localisation, from direct-write, with the principle of applying an electric potential between the nozzle and substrate, similar to EHD. Metal salt solutions (electrolytes) are used as the inks and they are brought close to the substrate inside a micronozzle. When the nozzle is close to the substrate a meniscus forms (dependent on humidity) between the nozzle and the substrate. The substrate is negatively charged with an oppositely charged electrode (thin wire) positioned inside the nozzle. By applying an electric field between these two electrodes the electroplating reaction will occur within the electrolyte meniscus. By properly designing the nozzles, the meniscus could be stabilised even while moving the nozzle, thereby facilitating the printing process while moving the nozzle [76]. Figures 4.3 A and B show examples of printed copper interconnects made using meniscus-confined electroplating. The

complex structures are printed by altering the shape of the nozzle to enable a meniscus to have vertical and horizontal components [76].

Another hybrid technique is force-controlled nanopipette electrodeposition or electroplating of locally dispensed ions in liquid, as it is also known [3, 53] . This technique has similarities to meniscus-confined electroplating in that again the electrochemical reduction is localised by using a nozzle to place the metal salt ink in the desired locations. An electrical potential is also used in this technique to cause the electrochemical reaction for deposition of the material, however, the electrode arrangement is altered. One electrode is attached to the substrate surface, as before, but the other one is positioned inside a bath of supporting electrolyte (the printing process occurs inside a liquid) [3].

There are two nozzle/electrode configurations that are used in this technique. The first uses a double barrelled nanopipette nozzle adapted from a scanning ion conductance microscope (SICM). The metal salt ink is passed down one of the barrels and the other is empty. The ink is forced down the nozzle where it can be placed in the required deposition position. The ions that flow out of the nozzle are electrochemically reduced in situ to the charged substrate plate [77]. An additional pair of electrodes are employed in this setup, one inside each barrel. The one in the empty barrel is used for SICM feedback and the one in the ink filled barrel is used to control the ink flux by electromigration [77]. Figure 4.3 C shows two printed columns where the freedom of movement has been utilised to create a zig-zag structure of the columns. These were printed using the nanopipette setup described.

The second configuration for this technique uses a slightly less obvious nozzle. Instead of a pipette nozzle, an atomic force microscope (AFM) tip is used. The tip has a nanochannel to allow flow of the ink to the tip apex for precise localisation. Again, there is an electrode attached to the substrate and another positioned in the electrolyte bath. Similar to before, the ionic ink exits the aperture and the electric potential causes the in situ electrochemical reduction to occur. No additional electrodes are required in this setup as the ink flow is regulated with a pressure controller and the feedback is provided by the force between the tip apex and the substrate, as used in contact mode AFM [53].Figure 4.3 D is a great example of the type of complex structures that this technique can create. This triple helical structure was printed using the AFM tip setup and demonstrates how intertwined structures can be produced using the layer by layer printing approach.

The advantage of force-controlled nanopipette electrodeposition/electroplating of locally dispensed ions in liquid is that there is a heightened freedom of movement of the tip [3]. In meniscus-confined electroplating, forming a meniscus in the desired location to generate complex structures can be difficult and special nozzles are required for specific printing pattern movements. With force-controlled nanopipette electrodeposition/electroplating of locally dispensed ions in liquid this limitation is overcome. Since there is no requirement to form a meniscus (just deposition of liquid ions to be reduced) complex structures can easily be formed layer by layer.

Overall, these hybrid techniques have been used to produce impressive structures with great potential to further advance the high-resolution 3D printing of many more materials.

4.4. Nozzle-less printing

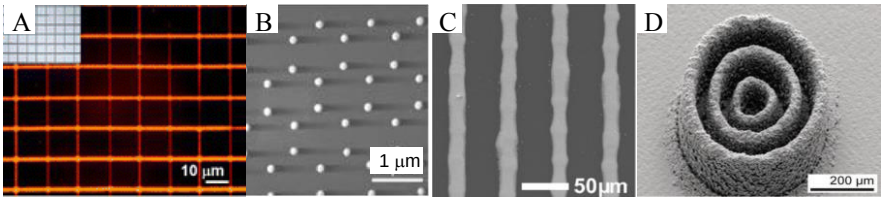

Figure 4.4: Exemplars of nozzle-less printing capabilities. (A) fluorescent microscope image of pyroelectrohydrodynamically printed polymeric fibers patterns; fibers are loaded with red fluorescent dye (inset shows a bright field image) [78]. (B) demonstrates how many single droplets can be printed in array patterns [79]. (C) illustrates how lines can also be printed with LIFT [36]. (D) gives an example of the complex structures that can be built layer by layer [3].

A number of functional structures have been printed using nozzle-less printing techniques and a wide swath of applications have also been shown to be feasible. Fig. 4.4A demonstrates the fluorescent polymeric fiber arrays printed using a pyroelectrohydrodynamic approach [78] and Fig. 4.4B demonstrates how LIFT can be used to print high-resolution fluorescent polymeric fiber structures and nanoparticle arrays[79]. By increasing the fluence rate and altering the movement of the substrate stage LIFT can be expanded to print lines as well (Fig. 4.4C). Complex high-resolution 3D structures can also be constructed by building up multiple layers of deposited material as shown in Fig. 4.4D.

Both LIFT and pyroelectrohydrodynamic printing clearly demonstrate a stronge potential for nozzle-free high-resolution printing. Current issues under intense research, especially for high-resolution printing, include a need for precise control of fluence, tight parameter window for stable operations etc.

4.5. Transfer printing

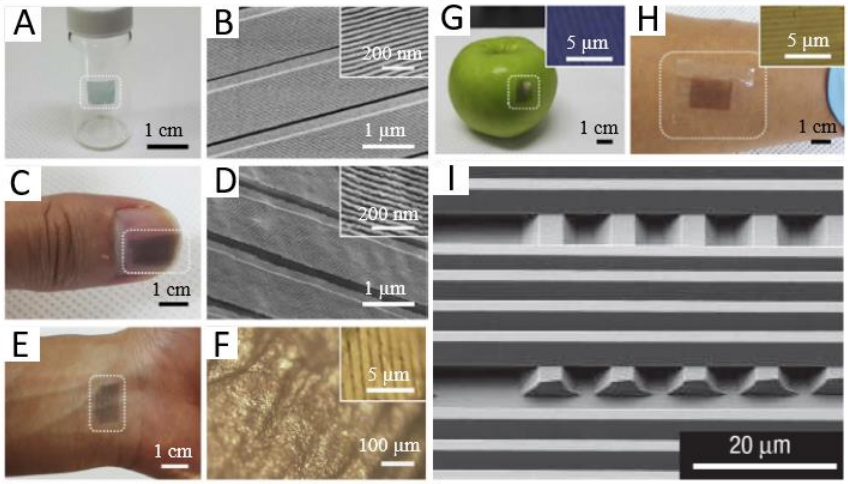

Figure 4.5: Exemplars of transfer printing capabilities. (A) and (B) demonstrate the ability to print 2D nanostructures onto a curved glass surface. (C) and (D) show how nanowires can also be printed onto a human fingernail and maintain the high-resolution print quality. (E) and (F) and (G) illustrate how transfer printing can also be used on soft materials such as skin and an apple [80]. (H) shows a flexible substrate with printed nanowires attached to human skin [80]. (I) is a stack of silicon ribbons demonstrating that 3D structures can be created with transfer printing [41].

Transfer printing has an advantage over other printing methods as it can be used safely on a multitude of different substrates and it is essentially a parallelised printing approach. Despite this versatility it still remains high-resolution with demonstrated ability to create nanometre feature sizes. Transfer printing is extremely good at printing 2D structures and though there are limitations to the 3D structures it can create, many are still possible.

The advances of transfer printing allow it to easily print on curved surfaces (Fig. 4.5A and B showing printing on glass) and many soft and flexible substrates as shown in Fig. 4.5C-F (examples of printing on finger nails (Fig. 4.5C and D) and human hands (Fig. 4.5 E)) [39]. The ability to create nanostructures on highly complex biological materials such as human skin (Fig. 4.5E), human fingernails (Fig. 4.5C) and fruit (Fig. 4.5G) without any pre-treatment of the surface has opened the door to many sensing applications. The approach has also been used to print structures on flexible substrates and be attached to skin [80]. This approach has also been utilised to make flexible quantum dot displays which have potential applications in many fields [39, 81]. The approach has also been shown to print multi-layered silicon ribbon stacks on silicon by making use of elastomeric stamps [41]. By harnessing this feature of transfer printing, and its high-resolution structures, *in vivo* biosensors could be developed. These printed structures could potentially detect biological signals and biomarkers [39].

4.6. Dip-pen nanolithography

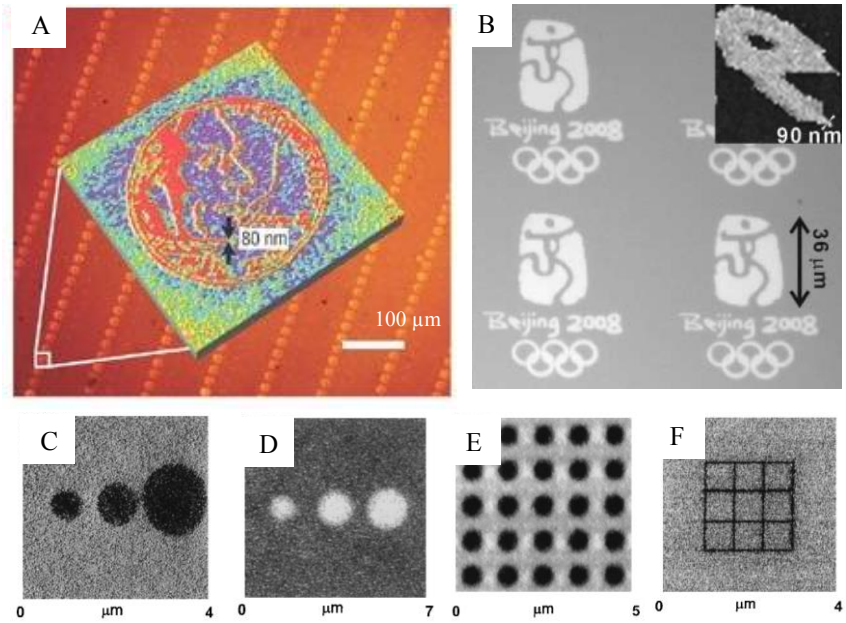

Figure 4.6: Exemplars of dip-pen nanolithography capabilities. (A) shows a part 55,000 dots printed with dip-pen nanolithography, within each dot is the image of an American 5 cent coin [27]. (B) Dip-pen printed logo of the Beijing Olympics, [82]. (C) and (D) are images of some of the first dots printed by dip-pen lithography. (E) is an array of dots on a gold substrate. (F) shows a printed grid, the width of each line is 100 nm [21].

Dip-pen nanolithography can create nanoscale resolution printed structures. This is illustrated quite well in Fig. 4.6A which shows a series of dots, each of which are comprise of a pattern shown in the inset [27]. The overall pattern consists of 55,000 dots. Each dot is in fact an image of an American 5 cent coin depicting Thomas Jefferson's face. As a further demonstration of the technique's resolution, Fig. 4.6B shows an image of a dip-pen printed logo of the 2008 Beijing Olympic Games. The small dimensions of the logo make it possible to fit 2,500 of them on a single grain of rice [82].

Fig. 4.6C and D are images of some of the fist dip-pen printed dot patterns reported by Mirkin's group. The different sizes of dots were achieved here by holding the tip in position for differing lengths of time. The longer the tip was held, the more of the ink could diffuse to the substrate. This technique can be replicated to create arrays of dots as seen in Fig. 4.6E. As well as dots, the group also showed a clear feasibility of printing grid patterns (Fig. 4.6F), with each line of the grid being ~100 nm wide and 2 µm long.

5. Summary and perspective

In this chapter we have presented a number of high-resolution 3D printing techniques where fluidics plays an important role. Challenges of high-resolution printing were discussed along with highlighting the formation and stability of droplets, jets and filaments (including liquid bridges), which are key features among different printing techniques. This also included discussion on relevant time and length scales in direct-write, EHD, nozzle-less, dip-pen and transfer printing techniques as well as hybrid approaches that employ more than one actuation mechanism for delivering printing "inks" to substrates. Next, the materials and fluidic features underpinning these techniques were discussed in detail. This included clear understanding of rheological, wetting and dynamic effects. Finally, a few exemplar printed structures were present to give a sense of the current state-of-the-art in fluidics assisted, high-resolution 3D printing.

From flexible electronics to healthcare, from smart photonics and plasmonics to precision micro-robotics and sensing, the potential applications of high-resolution 3D printing is truly enormous. Among other things, these techniques have a clear potential to serve as low-cost prototyping tools for novel micro/nanotechnology devices, in low-resource settings. From our discussions in this chapter, it is clear that a true synergy of material science, chemistry, fluidics and electronics is needed to push the frontiers of the technologies presented. In particular a lack of reliable fluid mechanics models for inks with complex rheological properties is an obvious area for future work. The serial nature of most 3D printing techniques puts a limit on throughput. One relatively obvious approach is to use serial approaches such as direct-write, EHD printing etc. to create master stamps for transfer printing which is highly parallelisable. Exciting new frontiers in printing soft materials and supporting scaffolds for biological niches [83-85] and functional organ-on-a-chip [86] applications are other medium term achievable goals, where initial feasibility has already been established. Combining serial printing with micro-molding approaches, e.g. soft lithography, can be another feasible route to overcome the issues in formulating an ideal ink for a particular material. Demonstrating ready and facile integration of printed devices e.g. miniature wearable sensors and biosensors on medical devices, is another exciting area of development. In addition, exploiting self-assembly principles in conjunction with printing can offer further design and manufacturing flexibility [87, 88]. Overall, with time, seamless integration of sophisticated machine learning techniques into high-resolution printing systems may also be a way to overcome the relative complexity of controlling multi-parameter optimisation that is often needed in successful realisation of high-resolution printed structures. Indeed, high-resolution 3D printing is a very unique and versatile topic for multi-disciplinary and high impact research.

6. Bibliography

1. Vaezi, M., H. Seitz, and S. Yang, *A review on 3D micro-additive manufacturing technologies.* International Journal of Advanced Manufacturing Technology, 2013. **67**: p. 1721-1754.
2. Ivanova, O., C. Williams, and T. Campbell, *Additive manufacturing (AM) and nanotechnology: promises and challenges.* Rapid Prototyping Journal, 2013. **19**: p. 353-364.
3. Hirt, L., et al., *Additive manufacturing of metal structures at the micrometer scale.* Advanced Materials, 2017. **29**: p. 1604211.
4. Fang, F., et al., *High-resolution 3D printing for healthcare underpinned by small-scale fluidics*. 2017, Woodhead Publishing.
5. De Gennes, P.-G., F. Brochard-Wyart, and D. Quéré, *Capillarity and wetting phenomena: drops, bubbles, pearls, waves*. 2013: Springer Science & Business Media.
6. Popov, Y.O., *Evaporative deposition patterns: Spatial dimensions of the deposit.* Physical Review E - Statistical, Nonlinear, and Soft Matter Physics, 2005. **71**.
7. Smay, J.E., J. Cesarano, and J.A. Lewis, *Colloidal inks for directed assembly of 3-D periodic structures.* Langmuir, 2002. **18**(14): p. 5429-5437.
8. Zhu, C. and J.E. Smay, *Catenary shape evolution of spanning structures in direct-write assembly of colloidal gels.* Journal of Materials Processing Technology, 2012. **212**(3): p. 727-733.
9. Onses, M.S., et al., *Mechanisms, capabilities, and applications of high-resolution electrohydrodynamic jet printing.* Small, 2015. **11**: p. 4237-4266.
10. Ru, C., et al., *A review of non-contact micro- and nano-printing technologies.* Journal of Micromechanics and Microengineering, 2014. **24**: p. 053001.
11. Park, J.-U., et al., *High-resolution electrohydrodynamic jet printing.* Nature Materials, 2007. **6**: p. 782-789.
12. Jaworek, A. and A. Krupa, *Classification of the modes of EHD spraying.* Journal of Aerosol Science, 1999. **30**: p. 873-893.
13. Basaran, O.A., *Small-scale free surface flows with breakup: Drop formation and emerging applications.* AIChE Journal, 2002. **48**: p. 1842-1848.
14. Collins, R.T., et al., *Electrohydrodynamic tip streaming and emission of charged drops from liquid cones.* Nature Physics, 2008. **4**: p. 149-154.
15. Galliker, P., et al., *Direct printing of nanostructures by electrostatic autofocussing of ink nanodroplets.* Nature Communications, 2012. **3**: p. 890.

16. Schirmer, N.C., et al., *On Ejecting colloids against capillarity from sub-micrometer openings: On-demand dielectrophoretic nanoprinting.* Advanced Materials, 2010. **22**(42): p. 4701-4705.
17. Hong, S., et al., *Dip-pen nanolithography*, in *Scanning Probe Microscopies Beyond Imaging*. 2006, Wiley-VCH Verlag GmbH & Co. KGaA: Weinheim, FRG. p. 141-174.
18. Kumar, S., *Liquid transfer in printing processes: Liquid bridges with moving contact lines.* Annual Review of Fluid Mechanics, 2015. **47**: p. 67-94.
19. Bostwick, J. and P. Steen, *Stability of constrained capillary surfaces.* Annual Review of Fluid Mechanics, 2015. **47**: p. 539-568.
20. Meyer, E., *Atomic force microscopy.* Progress in Surface Science, 1992. **41**: p. 3-49.
21. Piner, R.D., et al., *"Dip-pen" nanolithography.* Science, 1999. **283**(5402): p. 661-663.
22. Weeks, B.L., et al., *Effect of dissolution kinetics on feature size in dip-pen nanolithography.* Physical Review Letters, 2002. **88**: p. 255505.
23. Rozhok, S., R. Piner, and C.A. Mirkin, *Dip-pen nanolithography: What controls ink transport?* Journal of Physical Chemistry B, 2003. **107**: p. 751-757.
24. Sheehan, P.E. and L.J. Whitman, *Thiol diffusion and the role of humidity in "Dip Pen Nanolithography".* Physical Review Letters, 2002. **88**: p. 156104.
25. Stifter, T., O. Marti, and B. Bhushan, *Theoretical investigation of the distance dependence of capillary and van der Waals forces in scanning force microscopy.* Physical Review B, 2000. **62**: p. 13667-13673.
26. Schatz, G.C., *Using theory and computation to model nanoscale properties.* Proceedings of the National Academy of Sciences of the United States of America, 2007: p. 6885-6892.
27. Salaita, K., Y. Wang, and C.A. Mirkin, *Applications of dip-pen nanolithography.* Nature Nanotechnology, 2007. **2**: p. 145-155.
28. Lewis, J.A., *Colloidal processing of ceramics.* Journal of the American Ceramic Society, 2000. **83**(10): p. 2341-2359.
29. Ahn, B.Y., et al., *Omnidirectional printing of flexible, stretchable, and spanning silver microelectrodes.* Science, 2009. **323**: p. 1590-1593.
30. Gratson, G.M., M. Xu, and J.A. Lewis, *Microperiodic structures: Direct writing of three-dimensional webs.* Nature, 2004. **428**(6981): p. 386-386.
31. Berry, S.M., et al., *Characterization and modeling of direct-write fabrication of microscale polymer fibers.* Polymer, 2011. **52**(7): p. 1654-1661.
32. Lewis, J.A., *Direct ink writing of 3D functional materials.* Advanced Functional Materials, 2006. **16**: p. 2193-2204.
33. Ferraro, P., et al., *Dispensing nano-pico droplets and liquid patterning by pyroelectrodynamic shooting.* Nature Nanotechnology, 2010. **5**(6): p. 429-435.

34. Rogers, J.A. and U. Paik, *Nanofabrication: Nanoscale printing simplified.* Nature Nanotechnology, 2010. **5**(6): p. 385-386.
35. Ahmed, R. and T. Jones, *Optimized liquid DEP droplet dispensing.* Journal of Micromechanics and Microengineering, 2007. **17**(5): p. 1052.
36. In't Veld, B.H., et al., *Micro additive manufacturing using ultra short laser pulses.* CIRP Annals-Manufacturing Technology, 2015. **64**(2): p. 701-724.
37. Zywietz, U., et al., *Laser printing of silicon nanoparticles with resonant optical electric and magnetic responses.* Nature Communications, 2014. **5**: p. 3402.
38. Piqué, A., et al., *Laser 3D micro-manufacturing.* Journal of Physics D: Applied Physics, 2016. **49**(22).
39. Carlson, A., et al., *Transfer printing techniques for materials assembly and micro/nanodevice fabrication.* Advanced Materials, 2012. **24**(39): p. 5284-5318.
40. Michel, B., et al., *Printing meets lithography: Soft approaches to high-resolution patterning.* CHIMIA International Journal for Chemistry, 2002. **56**: p. 527-542.
41. Meitl, M.A., et al., *Transfer printing by kinetic control of adhesion to an elastomeric stamp.* Nature materials, 2006. **5**(1): p. 33.
42. Zaumseil, J., et al., *Three-dimensional and multilayer nanostructures formed by nanotransfer printing.* Nano Letters, 2003. **3**(9): p. 1223-1227.
43. Jeong, J.W., et al., *Nanotransfer printing with sub-10 nm resolution realized using directed self-assembly.* Advanced Materials, 2012. **24**(26): p. 3526-3531.
44. Batchelor, G.K., *An introduction to fluid dynamics*. 2000: Cambridge university press.
45. Kirby, B.J., *Micro-and nanoscale fluid mechanics: transport in microfluidic devices*. 2010: Cambridge University Press.
46. Duoss, E.B., et al., *Three-dimensional printing of elastomeric, cellular architectures with negative stiffness.* Advanced Functional Materials, 2014. **24**(31): p. 4905-4913.
47. Bhattacharjee, T., et al., *Writing in the granular gel medium.* Science Advances, 2015. **1**: p. e1500655-e1500655.
48. Chawla, K.K. and M. Meyers, *Mechanical behavior of materials*. 1999: Prentice Hall.
49. Miller, J.S., et al., *Rapid casting of patterned vascular networks for perfusable engineered three-dimensional tissues.* Nature Materials, 2012. **11**(9): p. 768-74.
50. Hinton, T.J., et al., *Three-dimensional printing of complex biological structures by freeform reversible embedding of suspended hydrogels.* Science advances, 2015. **1**(9): p. e1500758.
51. Tiwari, M.K., et al., *Highly liquid-repellent, large-area, nanostructured poly (vinylidene fluoride)/poly (ethyl 2-cyanoacrylate) composite coatings: particle filler effects.* ACS Applied Materials & Interfaces, 2010. **2**(4): p. 1114-1119.

52. Israelachvili, J.N., *Adhesion and wetting phenomena*, in *Intermolecular and Surface Forces*. 2011, Academic Press: San Diego. p. 415-468.
53. Hirt, L., et al., *Template-free 3D microprinting of metals using a force-controlled nanopipette for layer-by-layer electrodeposition.* Advanced Materials, 2016. **28**(12): p. 2311-2315.
54. Dong, Z., J. Ma, and L. Jiang, *Manipulating and dispensing micro/nanoliter droplets by superhydrophobic needle nozzles.* ACS Nano, 2013. **7**: p. 10371-10379.
55. Deegan, R.D., et al., *Capillary flow as the cause of ring stains from dried liquid drops.* Nature, 1997. **389**(6653): p. 827.
56. Einstein, A., *Investigations on the theory of the brownian movement*. 1956: Courier Corporation.
57. Shen, X., C.M. Ho, and T.S. Wong, *Minimal size of coffee ring structure.* Journal of Physical Chemistry B, 2010. **114**: p. 5269-5274.
58. Schirmer, N.C., et al., *On the principles of printing sub-micrometer 3D structures from dielectric-liquid-based colloids.* Advanced Functional Materials, 2011. **21**(2): p. 388-395.
59. McHale, G., et al., *Evaporation and the wetting of a low-energy solid surface.* The Journal of Physical Chemistry B, 1998. **102**(11): p. 1964-1967.
60. Hu, H. and R.G. Larson, *Marangoni effect reverses coffee-ring depositions.* Journal of Physical Chemistry B, 2006. **110**: p. 7090-7094.
61. Yunker, P.J., et al., *Suppression of the coffee-ring effect by shape-dependent capillary interactions.* Nature, 2011. **476**(7360): p. 308-311.
62. Derby, B., *Inkjet printing of functional and structural materials: Fluid property requirements, feature stability, and resolution.* Annual Review of Materials Research, 2010. **40**: p. 395-414.
63. *Ohnesorge number*, in *Encyclopedia of Microfluidics and Nanofluidics*, D. Li, Editor. 2008, Springer US: Boston, MA. p. 1513-1513.
64. Schiaffino, S. and A.A. Sonin, *Molten droplet deposition and solidification at low Weber numbers Transport and solidification phenomena in molten microdroplet pileup Molten droplet deposition and solidification at low Weber numbers.* Physics of Fluids, 1997. **9**: p. 3172-3187.
65. Stow, C. and M. Hadfield. *An experimental investigation of fluid flow resulting from the impact of a water drop with an unyielding dry surface*. in *Proceedings of the Royal Society of London A: Mathematical, Physical and Engineering Sciences*. 1981. The Royal Society.
66. Ahn, B.Y., et al., *Direct-write assembly of microperiodic planar and spanning ITO microelectrodes.* Chemical Communications, 2010. **46**: p. 7118-7120.
67. Muth, J.T., et al., *Embedded 3D printing of strain sensors within highly stretchable elastomers.* Advanced Materials, 2014. **26**: p. 6307-6312.
68. Skylar-Scott, M.A., S. Gunasekaran, and J.A. Lewis, *Laser-assisted direct ink writing of planar and 3D metal architectures.* Proceedings of the National Academy of Sciences, 2016. **113**(22): p. 6137-6142.

69. Lebel, L.L., et al., *Ultraviolet-assisted direct-write fabrication of carbon nanotube/polymer nanocomposite microcoils.* Advanced Materials, 2010. **22**(5): p. 592-596.
70. Richner, P., et al., *Full-spectrum flexible color printing at the diffraction limit.* ACS Photonics, 2016. **3**: p. 754-757.
71. Schneider, J., et al., *Site-specific deposition of single gold nanoparticles by individual growth in electrohydrodynamically-printed attoliter droplet reactors.* Nanoscale, 2015. **7**(21): p. 9510-9519.
72. Schneider, J., et al., *Electrohydrodynamic nanodrip printing of high aspect ratio metal grid transparent electrodes.* Advanced Functional Materials, 2016. **26**: p. 833-840.
73. Richner, P., et al., *Printable nanoscopic metamaterial absorbers and images with diffraction-limited resolution.* ACS Applied Materials & Interfaces, 2016. **8**: p. 11690-11697.
74. Schneider, J., et al., *A novel 3D integrated platform for the high-resolution study of cell migration plasticity.* Macromolecular Bioscience, 2013. **13**(8): p. 973-983.
75. Schirmer, N.C., et al., *Millimeter-wave on-chip solenoid inductor by on-demand three-dimensional printing of colloidal nanoparticles.* Applied Physics Letters, 2010. **97**(24): p. 243109.
76. Hu, J. and M.-F. Yu, *Meniscus-confined three-dimensional electrodeposition for direct writing of wire bonds.* Science, 2010. **329**(5989): p. 313-316.
77. Momotenko, D., et al., *Write-read 3D patterning with a dual-channel nanopipette.* ACS Nano, 2016. **10**(9): p. 8871-8.
78. Coppola, S., et al., *Tethered pyro-electrohydrodynamic spinning for patterning well-ordered structures at micro-and nanoscale.* Chemistry of Materials, 2014. **26**(11): p. 3357-3360.
79. Kuznetsov, A.I., et al., *Laser Fabrication of Large-Scale Nanoparticle Arrays for Sensing Applications.* Acs Nano, 2011. **5**(6): p. 4843-4849.
80. Jeong, J.W., et al., *High-resolution nanotransfer printing applicable to diverse surfaces via interface-targeted adhesion switching.* Nature communications, 2014. **5**: p. 5387.
81. Kim, T.-H., et al., *Full-colour quantum dot displays fabricated by transfer printing.* Nature Photonics, 2011. **5**: p. 176-182.
82. Huo, F., et al., *Polymer pen lithography.* Science, 2008. **321**(5896): p. 1658-1660.
83. Gui, L. and L.E. Niklason, *Vascular tissue engineering: building perfusable vasculature for implantation.* Current opinion in chemical engineering, 2014. **3**: p. 68-74.
84. Gattazzo, F., A. Urciuolo, and P. Bonaldo, *Extracellular matrix: a dynamic microenvironment for stem cell niche.* Biochimica et Biophysica Acta (BBA)-General Subjects, 2014. **1840**(8): p. 2506-2519.
85. Ou, K.-L. and H. Hosseinkhani, *Development of 3D in vitro technology for medical applications.* International journal of molecular sciences, 2014. **15**(10): p. 17938-17962.

86. Murphy, S.V. and A. Atala, *3D bioprinting of tissues and organs.* Nature biotechnology, 2014. **32**(8): p. 773-785.
87. Gladman, A.S., et al., *Biomimetic 4D printing.* Nature Materials, 2016. **15**(4): p. 413-418.
88. Zhang, Y., et al., *Printing, folding and assembly methods for forming 3D mesostructures in advanced materials.* Nature Reviews Materials, 2017. **2**: p. 17019.